

Test particle acceleration in explosive magnetohydrodynamic reconnection

B. Ripperda^{*1}, O. Porth², C. Xia¹ and R. Keppens¹

¹Centre for mathematical Plasma Astrophysics, Department of Mathematics, KU Leuven, Celestijnenlaan 200B, B-3001 Leuven, Belgium

²Institut für Theoretische Physik, Max-von-Laue-Str. 1, D-60438 Frankfurt, Germany

December 4, 2016

Abstract

Magnetic reconnection is the mechanism behind many violent phenomena in the universe. We demonstrate that energy released during reconnection can lead to non-thermal particle distribution functions. We use a method in which we combine resistive magnetohydrodynamics (MHD) with relativistic test particle dynamics. Using our open-source grid-adaptive MPI-AMRVAC software, we simulate global MHD evolution combined with test particle treatments in MHD snapshots. This approach is used to evaluate particle acceleration in explosive reconnection. The reconnection is triggered by an ideal tilt instability in two-and-a-half dimensional (2.5D) scenarios and by a combination of ideal tilt and kink instabilities in three-dimensional (3D) scenarios. These instabilities occur in a system with two parallel, adjacent, repelling current channels in an initially force-free equilibrium, as a simplified representation of flux ropes in a stellar magnetosphere. The current channels undergo a rotation and a separation on Alfvénic timescales, forming secondary islands and nearly singular current sheets. In these reconnection areas particles are efficiently accelerated up to high energy. In the low plasma- β settings used, the dynamics of the particles can be approximated by the relativistic guiding centre approximation. Both in 2.5D and 3D simulations non-thermal distributions are formed in (up to tearing unstable) current sheets in the nonlinear regime. We analyse the drift motion and the energetics of the charged particles for proton-electron plasmas, which is relevant for particle acceleration in solar flares and in other, more exotic astrophysical phenomena, like black hole flares, magnetar magnetospheres and pulsar wind nebulae.

1 Introduction

Astrophysical plasmas are systems in which physical phenomena are coupled from macroscopic to microscopic scales in space and time. The complexity

^{*}E-mail: bart.ripperda@kuleuven.be

of modelling such a system comes from the coupling of relatively slow macroscopic processes and faster and smaller processes on the particle scale. One of the most important processes exhibiting these distinctive differences, which are tightly coupled on the different scales, is magnetic reconnection. The change of topology of the magnetic field configuration on large scales is described by magnetohydrodynamics (MHD) and the dissipation at small scales is described by kinetic (particle) theory. The MHD approach covers the overall scales and energetics of the system but does not give any information on particle dynamics. Kinetic approaches fully describe the microscopic scale, but are too costly to cover full astrophysical systems.

There are currently many efforts to overcome this issue and to bridge the gap between the two approaches. Fully kinetic particle-in-cell (PIC) codes (e.g. Noguchi et al. 2007, Guo et al. 2015 for relativistic plasmas and Markidis and Lapenta 2011, Li et al. 2015 for non-relativistic plasmas) treat both electrons and ions as particles and iteratively move these particles and update the electromagnetic fields accordingly. This is the most complete method, but as mentioned, it has to resolve the microscopic scales of the plasma, demanding extreme computational cost. Another approach is to treat a part of the plasma as a fluid and another (typically non-thermal) ensemble of particles with a PIC technique. The separation can be done based on the energy of the particles (e.g. Bai et al. 2015) or based on locating zones in which kinetic effects may play an important role (e.g. Daldorff et al. 2014, Markidis et al. 2014, Markidis et al. 2015, Tóth et al. 2016, Vaidya et al. 2016). The caveat in this approach is that there has to be a clear separation of MHD scale physics and kinetic scale physics, either based on energy or location, to choose where kinetic physics are incorporated or not. This can be problematic for plasmas with reconnection occurring over the whole domain and when a majority of particles is accelerated up to non-thermal energies, since then the whole domain has to be treated with the particle-in-cell method.

In this paper, we consider a more traditional approach, in which we treat electrons and ions as test particles embedded in a thermal (MHD) plasma. The test particles only respond to the MHD fields in a kinetic, passive way. They are guided by the electromagnetic fields without giving feedback to these fields. For typical plasma parameters used, the gyroradius can be calculated and compared to the typical size over which the fields change. If this size is very large compared to the gyroradius, the guiding center approximation (GCA) can be applied, neglecting the gyration of test particles. Typical parameters for low plasma- β plasma in the solar corona are, for magnetic field magnitude $B = 0.03T$, temperature $T = 10^6 K$, plasma- $\beta = 0.0004$, number density $n = 10^{16} m^{-3}$, thermal speed $v_{th,e} = 5.5 \times 10^7 ms^{-1}$ for electrons and $v_{th,p} = 1.3 \times 10^6 ms^{-1}$ for protons, both giving a thermal Lorentz factor of $\gamma \approx 1$ (Goedbloed and Poedts 2004). In solar coronal plasmas the typical gyroradius of the particles ($R_L = 10^{-3}m$ for electrons and $R_L = 4.4 \times 10^{-2}m$ for protons) is much smaller than the length scales over which MHD fields evolve and typical timescales of the particle dynamics are much smaller than dynamic timescales of the MHD, making the test particle approach valid. This method has been widely used to study test particle acceleration in the solar corona (Rosdahl and Galsgaard 2009, Gordovskyy et al. 2014, Zhou et al. 2015, Zhou et al. 2016, Pinto et al. 2016) and recently to study transport of high-energy particles in pulsar wind nebulae (Porth et al. 2016). We use relativistic test particles in MHD reconnection setups to study non-thermal

emission in magnetically dominated (low plasma- β), non-relativistic plasmas.

The detailed physics of magnetic reconnection, including its initiation mechanism, energy conversion, and efficient acceleration of particles is not well understood. Ideal magnetohydrodynamic instabilities can cause the topology of the magnetic field to change and are therefore one of the most common routes to disrupt a magnetically dominated plasma. Current-driven MHD instabilities, involving interacting currents are a viable way to achieve this, but the main question is how to initialise such a setup and locate potential reconnection regions in which particles accelerate based on MHD simulations. A typical plasma process leading to an instability is the formation of current filaments, which interact in a number of ways, e.g. they may attract, merge or repel. Attracting currents result in the ideal coalescence instability (Finn and Kaw 1977; Longcope and Strauss 1993), in which the currents move toward each other and merge. We present a problem closely related to the coalescence instability, in which oppositely directed currents repel one another. In this so-called tilt instability the poloidal field distribution forms islands that repel, causing fast reconnection and development of nearly-singular current layers. Reconnection caused by repelling currents in a two-dimensional (2D) force-free equilibrium has been studied by Richard et al. (1990). We focus on parallel, straight current channels in both force-free and non-force-free equilibrium configurations in two-and-a-half-dimensional (2.5D) and three-dimensional (3D) scenarios. This setup represents the top parts of adjacent flux ropes as seen in coronae of stars. The tilt instability may be accessible if the flux ropes develop anti-parallel currents. In 3D scenarios the currents are liable to an additional kink instability that interacts with the tilt instability, which was studied in a non-force-free equilibrium setting in Keppens et al. (2014). The kink instability redistributes the poloidal field and this is known to relate to violent plasmas eruptions in astrophysical systems. The kink instability is typically triggered by strong twist in the magnetic field, which in 3D scenarios is provided by the tilting and rotating of the current channels. Current channels undergoing a tilt and/or kink instability typically undergo a linear phase in which kinetic energy grows exponentially, after which the magnetic field in the current channels starts reconnecting with the background magnetic field (Browning et al. 2008). As a result, stored magnetic energy is released and converted into other forms of energy. Recently, it has been shown that the energy released during reconnection, initiated by a kink instability, may lead to plasma heating (Pinto et al. 2015). This impulsive plasma heating can result in particle acceleration leading to non-thermal X-ray emission (Gordovskyy et al. 2014).

On the fundamental particle level, the energy released by magnetic reconnection goes into the kinetic energy of individual particles, however investigating how instabilities lead to large scale dynamics in astrophysical systems is traditionally done with an MHD approach. The energetics of the plasma can be split into the part relevant at the fluid level plus non-thermal particle distributions. The macroscopic approximation describes the time dependent evolution of magnetic fields, bulk velocity fields and density of the plasma. This approach is valid when the plasma is in local thermodynamic equilibrium and when the mean free path of the particles present in the plasma is much smaller than the characteristic MHD length scale. During reconnection this approximation breaks down. However, reconnection can be studied in the MHD context by a parametrisation approximating particle interactions on scales below the characteristic MHD

length scales through viscosity and resistivity. That, however, does not give any information on particle acceleration within reconnection regions. Nor does it include the effect of accelerated particles on the global fields. To study the former of these two shortcomings of MHD, we adopt a test particle approach, in which particle dynamics are traced in the global fields obtained from snapshots of the high resolution MHD runs. We explore how effective particle accelerations can be achieved within the tilt and kink driven violent formation of current sheets with multiple reconnection sites. This is relevant for solar flares, but also for more extreme settings encountered in strongly magnetized astrophysical plasmas characterized with anti-parallel current systems. Flares from astrophysical objects require energy from macroscopic scales to be transferred to the microscopic scales on which particles are accelerated. Here we address plasmas with particle kinetic energy dominating over magnetic energy. This is indicated by the so called σ -parameter, $\sigma \ll 1$, meaning that the fields in the plasma are non-relativistic. In contrast to high-energy, relativistic plasma environments, in solar flares one can ignore radiation emitted promptly during the reconnection process. In these environments, the time energetic particles spend in the reconnection region is usually much shorter than their radiative cooling time (Uzdensky 2016). This justifies a test particle approach, in which radiation back-reaction on reconnection dynamics, energetics and particle acceleration is ignored. Particle acceleration due to idealised current driven instabilities in magnetically dominated, relativistic plasmas has been studied with both MHD and particle approaches in Lyutikov et al. (2016).

We use high-resolution simulations both with a fixed grid and with adaptive mesh refinement (AMR) to study the evolution of the adjacent, repelling current channels through the tilt and kink instabilities in 2.5D and 3D configurations. For test particle simulations we make use of the latest addition to the MPI-AMRVAC code functionality to also dynamically evolve particle populations, during MHD evolutions. The MHD equilibrium setup and the numerical methods employed are described in detail in Section 2.1 and the test particle approach is discussed in Section 2.2. In Section 3 2.5D MHD simulations are discussed, in Section 4 we discuss 3D simulations and the effect of the kink instability on the tilt instability. In Section 5 the behaviour of test particles in 2.5D MHD snapshots is discussed.

2 Numerical setup

2.1 MHD setup and model description

We simulate two parallel, adjacent, repelling current channels in a square region $[-3L, 3L] \times [-3L, 3L]$ in Cartesian coordinates (x, y) with vector z components orthogonal to the plane in both the 2.5D and 3D setups. A typical unit of length for the astrophysical systems under consideration is $L = 10 \cdot 10^6 m$. This length scale will be used to scale the MHD results in accordance with the dimension-full particle simulations. In equilibrium the currents are described by the initial conditions for the flux function $\psi_0(x, y)$

$$\psi_0(x, y) = \begin{cases} \frac{2}{j_0^l j_0^r} J_1(j_0^l r) \cos(\theta) & \text{for } r < 1. \\ (r - \frac{1}{r}) \cos(\theta) & \text{for } r \geq 1. \end{cases} \quad (1)$$

where we use polar coordinates in the (x, y) plane with $(r, \theta) = (\sqrt{x^2 + y^2}, \arctan(y/x))$, J_1 is the Bessel function of the first kind and $j_0^1 \approx 3.831706$ is the first root of J_1 . From the flux function, the in-plane magnetic field components of $\mathbf{B} = \nabla\psi_0 \times \hat{\mathbf{z}} + B_z \hat{\mathbf{z}}$ are found to be

$$\begin{aligned} B_x &= +\frac{\partial\psi_0}{\partial y}, \\ B_y &= -\frac{\partial\psi_0}{\partial x}. \end{aligned} \quad (2)$$

This equilibrium results in a current distribution with two anti-parallel current channels, where $J_z = (\nabla \times \mathbf{B})_z = -\nabla^2 \psi_0$. In one half of the unit circle $J_z > 0$ and in the other half $J_z < 0$. An ideal MHD equilibrium can be established in two ways. One option is to find a pressure gradient balancing the Lorentz force

$$p(x, y) = \begin{cases} p_0 + \frac{(j_0^1)^2}{2}(\psi_0(x, y))^2 & \text{for } r < 1. \\ p_0 & \text{for } r \geq 1. \end{cases} \quad (3)$$

and an additional parameter $B_z = B_{z0}$, to be chosen freely to analyse different cases of plasma β , indicating the strength of the magnetic field component in the z -direction. A second option is to employ a force-free magnetic field with spatially varying, vertical component $B_z(x, y)$ and a uniform plasma pressure p_0 such that the Lorentz force $\mathbf{J} \times \mathbf{B} = \nabla p = 0$, here

$$B_z(x, y) = \begin{cases} (j_0^1)(\psi_0(x, y)) & \text{for } r < 1. \\ 0 & \text{for } r \geq 1. \end{cases} \quad (4)$$

The constant pressure can be chosen freely to analyse different cases of plasma β . In both cases there are no currents in the region $r \geq 1$ initially and the pressure is constant here. Note that a force-free configuration is more realistic in astrophysical context since the structure and dynamics of the corona are magnetically dominated. Magnetic forces are so dominant in most areas of the corona that all other forces, including gravity and plasma pressure gradients are negligible (Schrijver et al. 2008; Wiegmann and Sakurai 2012). The vertical magnetic field component is strong inside the current channels and zero outside the current channels, which is also more realistic physically than a setup with a constant and uniform vertical magnetic field component both in the current channels and in the background. Another advantage is that a force-free configuration allows us to explore the more realistic low plasma- β regime.

The set of resistive, compressible 3D MHD equations is solved,

$$\partial_t \rho + \nabla \cdot (\mathbf{u}\rho) = 0, \quad (5)$$

$$\partial_t(\rho\mathbf{u}) + \nabla \cdot (\mathbf{u}\rho\mathbf{u} - \mathbf{B}\mathbf{B}) + \nabla(p + \mathbf{B}^2/2) = 0, \quad (6)$$

$$\partial_t(e) + \nabla \cdot (\mathbf{u}e - \mathbf{B}\mathbf{B} \cdot \mathbf{u} + \mathbf{u}(p + \mathbf{B}^2/2)) = \nabla \cdot (\mathbf{B} \times \eta \mathbf{J}), \quad (7)$$

$$\partial_t(\mathbf{B}) + \nabla \cdot (\mathbf{u}\mathbf{B} - \mathbf{B}\mathbf{u}) = -\nabla \times (\eta \mathbf{J}), \quad (8)$$

where \mathbf{u} is the bulk fluid velocity field, e is the total energy density, $\mathbf{J} = \nabla \times \mathbf{B}$ the total current density and total pressure is $p = (\Gamma - 1)(e - \rho\mathbf{u}^2/2 - \mathbf{B}^2/2)$.

The resistivity parameter is set to $\eta_0 = 10^{-4}$. We apply two different resistivity models. A uniform resistivity η_0 and an anomalous, current dependent

resistivity (e.g. Otto 2001)

$$\eta(j) = \eta_0 S(j - j_c) \quad (9)$$

with $S(\xi)$ a step function, which is unity for $\xi \geq 0$ and zero otherwise. The critical current density j_c is set such that the resistivity is nonzero for values larger the equilibrium current density, such that there is no diffusion in the equilibrium, but that the threshold is much lower than the peak current reached. Different values of j_c will be used to see the effect on the diffusion of the gradient of the magnetic field, and hence, the current.

We will quantify differences between the two different equilibrium setups, and we will vary both B_{z0} and p_0 to model different plasma β conditions. In both cases we set the density ρ to unity initially and the ratio of specific heats $\Gamma = 5/3$. In the non-force-free case we fix $p_0 = 1/\Gamma$ and vary B_{z0} over a range of 0 to 5 and in the force-free case, we vary p_0 over a range of $0.01/\Gamma$ to $5/\Gamma$. The normalisation used implies the sound speed outside the current channels as the unit of speed, the radius of the double current channel as the unit of length and the density to fix the unit of mass. We employ magnetic units where $\mu_0 = 1$.

Both equilibrium setups are unstable to ideal MHD instabilities with Alfvénic growth rates (Richard et al. 1990). To trigger these instabilities, the equilibrium is perturbed by an incompressible velocity field

$$\begin{aligned} u_x &= +\frac{\partial\phi_0}{\partial y} [\times \sin(k_z z)], \\ u_y &= -\frac{\partial\phi_0}{\partial x} [\times \sin(k_z z)], \\ u_z &= 0, \end{aligned} \quad (10)$$

where $\phi_0(x, y) = \xi \exp(-x^2 - y^2)$ is the stream function with a perturbation amplitude $\xi = 0.0001$. In case of a 3D simulation, $k_z = 2\pi/L_z$ with $L_z = 6$ the typical simulation box size and $z \in [-3L, 3L]$, again with $L = 10 \cdot 10^6 m$. In all 2.5D simulations, the dependence on the z coordinate doesn't apply for the perturbation field. A linear stability analysis for 2D incompressible MHD, based on an energy principle, has been carried out by Richard et al. (1990), showing that the equilibrium is unstable to a tilt instability in the (x, y) -plane. It is shown by Keppens et al. (2014) that two additional effects come into play in a non-force-free 3D setup, namely that the field lines can bend with respect to the vertical direction and that the current channels may be unstable to an ideal kink instability, depending on typical magnetic field strengths and system size. If the z -component of the magnetic field is strong enough, the magnetic tension may also stabilize or delay kink deformations and even prevent tilt development in the (x, y) plane.

The tilt instability is an ideal MHD instability, from which it can be concluded that the resistivity has little effect on the (linear) onset phase of the instability (Richard et al. 1990). Once the instability develops and the physics becomes naturally nonlinear, it allows for fast reconnection of the field lines. To show the difference between numerical resistivity and the implemented physical resistivity, we conduct simulations with varying grid resolutions, which mainly becomes important in the chaotic reconnection regime.

The boundary conditions in the (x, y) plane are chosen such that there is a zero gradient. A continuous extrapolation, from the closest inner mesh cell

value to all of the ghost cells, of the primitive variables ρ , \mathbf{v} and p is adopted. In the ghost cells, the magnetic field fixes the analytic profiles from the equilibrium and subsequently employs a second order, central difference evaluation of $\nabla \cdot \mathbf{B}$, to correct the component normal to the boundary. This approach was shown to work well by Keppens et al. (2014) for a non-force-free case and will therefore be used here in combination with a diffusive approach on the monopole error control. We use the same discretisation to quantify the divergence of the magnetic field and then add it as a diffusion part to the induction equation (8) as $\nabla((\Delta x)^2 \nabla \cdot \mathbf{B})$. For the integration we use a three-step Runge-Kutta-type scheme with a third-order limiter and a Harten-Lax-van Leer (HLL) flux prescription (Čada and Torrilhon 2009; Porth et al. 2014).

Resolutions of 300^2 up to 4800^2 are used, where the higher resolutions are achieved by employing 4 – 5 AMR grid levels. Runs with a uniform grid at the highest resolutions have confirmed that numerical instabilities due to negative pressure development at refinement boundaries are avoided, even for the lowest β case. In the 3D setups, we use a base resolution of 150^3 with 1–2 AMR grid levels to achieve either 150^3 or 300^3 effective resolution respectively. In Table 1 we list the most important parameters for the different cases (where *ff* indicates a force-free equilibrium configuration and *nff* a non-force-free equilibrium configuration and the addition of *AR* indicates that an anomalous resistivity model is used with critical current density threshold j_c), quantifying typical plasma conditions. We calculate mean initial (equilibrium) values of prevailing current density \bar{J} , plasma beta $\bar{\beta}$ and temperature \bar{T} for both the non-force-free and force-free cases with different choices of B_{z0} and p_0 . The mean value for a scalar is computed as

$$\bar{f}^{\pm} \equiv \frac{\iint_{j_z(t=0) \gtrless 0} f dx dy}{\iint_{j_z(t=0) \gtrless 0} dx dy} \quad (11)$$

over the current cross-section. The \pm stands for the positive or negative current density in the z -direction, respectively. Initially, the area in the denominator is exactly half the unit circle ($\pi/2$), however, at later times we cannot depend purely on the sign of $J_z(t)$ due to dynamic changes in the current channels. As a solution, we advect a tracer which identifies the displaced location of the positive and negative current channels. This tracer also allows us to quantify energetics in either one of the current channels.

2.2 Relativistic test particle dynamics and the guiding centre approximation

The MHD approach as described in Section 2.1 provides the macroscopic time dependent evolution of the plasma, in terms of the magnetic field, density, pressure and bulk velocity field. The current distribution and the electric field can be calculated from these fields. For a plasma in local thermodynamic equilibrium and on typical length scales much larger than the mean free path of particles, the large scale evolution is well described by these macroscopic parameters. If reconnection takes place, localised, near-singular current sheets form and sub-MHD-scale physics becomes important. The motion of charged particles, allowed to reach high energies, in electromagnetic fields is described

Table 1: The simulated cases and several characteristic parameters.

Run	p_0	\bar{B}_z	$\bar{\beta}$	effective resolution	j_c	\bar{T}	γ_{tilt}
A2dnff	1.0/ Γ	0.0	12.7	2400 ²	0	1.6	1.5000
B2dnff	1.0/ Γ	0.1	5.8	2400 ²	0	1.6	1.4969
C2dnff	1.0/ Γ	0.5	2.6	2400 ²	0	1.6	1.4893
D2dnff	1.0/ Γ	1.0	1.4	2400 ²	0	1.6	1.4842
E2dnff	1.0/ Γ	5.0	0.12	2400 ²	0	1.6	1.3565
f2dff	0.01/ Γ	1.14	0.04	300 ²	0	0.006	
F2dff	0.01/ Γ	1.14	0.04	2400 ²	0	0.006	1.6578
FF2dff	0.01/ Γ	1.14	0.04	4800 ²	0	0.006	
G2dff	0.05/ Γ	1.14	0.18	2400 ²	0	0.03	1.6510
H2dff	0.1/ Γ	1.14	0.36	2400 ²	0	0.06	1.6492
I2dff	0.5/ Γ	1.14	1.8	2400 ²	0	0.3	1.5793
J2dff	1.0/ Γ	1.14	4.0	2400 ²	0	0.6	1.4968
K2dff	5.0/ Γ	1.14	18.1	2400 ²	0	3.0	1.4018
F2dffAR	0.01/ Γ	1.14	0.04	2400 ²	12	0.006	1.8206
F2dffAR2	0.01/ Γ	1.14	0.04	2400 ²	500	0.006	1.6404
G2dffAR	0.05/ Γ	1.14	0.18	2400 ²	12	0.03	1.8012
Run	p_0	\bar{B}_z	$\bar{\beta}$	resolution	j_c	\bar{T}	K_{cr}
A3dnff	1.0/ Γ	0.0	12.7	300 ³	0	1.6	∞
B3dnff	1.0/ Γ	0.1	5.8	300 ³	0	1.6	43.5
C3dnff	1.0/ Γ	0.5	2.6	300 ³	0	1.6	8.7
D3dnff	1.0/ Γ	1.0	1.4	300 ³	0	1.6	4.35
E3dnff	1.0/ Γ	5.0	0.12	300 ³	0	1.6	0.87
f3dff	0.01/ Γ	1.14	0.04	150 ³	0	0.006	3.83
F3dff	0.01/ Γ	1.14	0.04	300 ³	0	0.006	3.83
G3dff	0.05/ Γ	1.14	0.18	300 ³	0	0.03	3.83
H3dff	0.1/ Γ	1.14	0.36	300 ³	0	0.06	3.83
I3dff	0.5/ Γ	1.14	1.8	300 ³	0	0.3	3.83
J3dff	1.0/ Γ	1.14	4.0	300 ³	0	0.6	3.83
K3dff	5.0/ Γ	1.14	18.1	300 ³	0	3.0	3.83
F3dffAR	0.01/ Γ	1.14	0.04	300 ³	12	0.006	3.83
G3dffAR	0.05/ Γ	1.14	0.18	300 ³	12	0.03	3.83

Note: The leftmost column labels the various runs, ff and nff indicate force-free and non-force-free equilibrium configurations respectively. The right column quantifies the tilt mode growth rate for 2.5D runs and the liability to a kink instability for 3D runs (see text for details).

by a relativistic, tensorial equation of motion (e.g. Landau and Lifshitz 1960):

$$\frac{d^2 x_i}{d\tau^2} = \frac{q}{mc} F_{ik} \frac{dx^k}{d\tau}, \quad (12)$$

in which the Einstein summation convention is used and with $x_i = (ct, \mathbf{r})$ the particles position in spacetime, c the speed of light in vacuum and τ the proper time. F_{ik} is the electromagnetic field tensor consisting of the components of \mathbf{B} and \mathbf{E} . The equations can be split by choosing a certain frame of reference. The first three components of equation (12) are similar to the equation of motion $d\mathbf{p}/dt = q(\mathbf{E} + \mathbf{v} \times \mathbf{B}/c)$, in three-space, where $\mathbf{p} = m_0 \gamma \mathbf{v}$ is the relativistic momentum, with m_0 the rest mass of the particle and $\gamma = 1/\sqrt{1 - v^2/c^2}$ the Lorentz factor, q the particles charge, \mathbf{E} and \mathbf{B} the electromagnetic fields guiding the particle and \mathbf{v} the particle velocity. These equations are solved in Porth et al. (2016) for test particles in pulsar wind nebulae. The fourth component of (12) is the rate of change of energy of the particle. The microscopic approach of treating individual particles has to be equivalent to the macroscopic equations of MHD. This can be shown by deriving the MHD equations from the microscopic equations of motion, see for instance Clemmow and Dougherty (1969).

To simplify the description of the (relativistic) motion of a charged particle in an electromagnetic field one can express the position of the particle in terms of variables which represent the gyration around the magnetic field lines and the motion of the point around which the particle gyrates, called the guiding centre (Northrop 1963, Northrop 1964). The gyration can be separated from the motion of the guiding centre under the assumption that the electromagnetic field varies only over an interval of spacetime much larger than the gyration radius, and that the particle undergoes many gyration cycles before the field has varied significantly in space, respectively. More specifically, this guiding centre approximation is based on an expansion in powers of $\frac{1}{\Omega} \frac{d}{dt}$, with $\Omega = qB/m_0$ the Larmor frequency and B the magnitude of the magnetic field. The gyration at frequency Ω is averaged out, for a particle with gyroradius

$$R_L = \frac{\gamma m_0 v_\perp}{Bq}, \quad (13)$$

and v_\perp the velocity component perpendicular to the magnetic field. A typical gyration radius for electrons and protons can be calculated and compared to the typical size over which the fields change. If this size is very large compared to the gyration radius, the guiding centre approximation gives accurate results, comparable to the solution given by the full equation of motion (12).

If the guiding centre equations are written in a relativistic, covariant form, following from the expansion of (12), the electric fields are allowed to have a component parallel to the magnetic field. These parallel electric fields typically produce high energy particles with a small pitch angle $\alpha = \arctan(v_\perp/v_\parallel)$, the angle between the velocity vector of a particle and the unit vector parallel to the magnetic field $\hat{\mathbf{b}}$. Furthermore, due to several drift terms in the equation of motion, particles are allowed to move in a direction not parallel to the magnetic field lines guiding them (hence, possibly obtaining a larger pitch angle). The drift velocities are allowed to approach the speed of light, removing restrictions on the electric field strength. We assume that the variations of the field in which the particle moves, in space and time, are sufficiently slow such that it changes

only during intervals of proper time which are long compared to a gyration period. This is the case for non-relativistic plasmas with $\sigma \equiv B^2/4\pi\rho_0 c^2 \ll 1$ and hence non-relativistic Alfvén velocities, with $\rho_0 c^2$ the rest energy density of the plasma. In the case of slowly varying global fields the temporal variations of the fields are much smaller than the variations due to particle motion and hence, temporal derivatives in the guiding centre equations can be neglected. This reduces computing time further without compromising accuracy. Using these approximations and neglecting the higher order terms of the expansion, allows to write an equation which solely depends on the guiding centre position of the particle. In the solar corona this assumption is accurate, however in flares emerging from black holes or neutron stars, the global flow may be strongly relativistic and this assumption breaks down. The complete solution for the guiding centre still depends on the particular electromagnetic field and its spatial derivatives as obtained from MHD. After choosing a specific hypersurface to split the spacetime components, applying the approximations to the guiding centre equations gives three equations, corresponding to the spatial components of (12), describing the (change in) guiding centre position \mathbf{R} , parallel relativistic momentum $p_{\parallel} = m_0 \gamma v_{\parallel}$ and relativistic magnetic moment $\mu_r = m_0 \gamma^2 v_{\perp}^2 / 2B$ in three-space (Vandervoort 1960)

$$\begin{aligned} \frac{d\mathbf{R}}{dt} &= \frac{(\gamma v_{\parallel})}{\gamma} \hat{\mathbf{b}} + \frac{\hat{\mathbf{b}}}{B \left(1 - \frac{E_{\perp}^2}{B^2}\right)} \times \left\{ - \left(1 - \frac{E_{\perp}^2}{B^2}\right) c \mathbf{E} + \right. \\ &\quad \frac{cm_0 \gamma}{q} \left(v_{\parallel}^2 (\hat{\mathbf{b}} \cdot \nabla) \hat{\mathbf{b}} + v_{\parallel} (\mathbf{u}_{\mathbf{E}} \cdot \nabla) \hat{\mathbf{b}} + v_{\parallel} (\hat{\mathbf{b}} \cdot \nabla) \mathbf{u}_{\mathbf{E}} + (\mathbf{u}_{\mathbf{E}} \cdot \nabla) \mathbf{u}_{\mathbf{E}} \right) + \\ &\quad \left. \frac{\mu_r c}{\gamma q} \nabla \left[B \left(1 - \frac{E_{\perp}^2}{B^2}\right)^{1/2} \right] + \frac{v_{\parallel} E_{\parallel}}{c} \mathbf{u}_{\mathbf{E}} \right\}, \end{aligned} \quad (14)$$

$$\begin{aligned} \frac{d(m_0 \gamma v_{\parallel})}{dt} &= m_0 \gamma \mathbf{u}_{\mathbf{E}} \cdot \left(v_{\parallel}^2 (\hat{\mathbf{b}} \cdot \nabla) \hat{\mathbf{b}} + v_{\parallel} (\mathbf{u}_{\mathbf{E}} \cdot \nabla) \hat{\mathbf{b}} + \right. \\ &\quad \left. q E_{\parallel} - \frac{\mu_r}{\gamma} \hat{\mathbf{b}} \cdot \nabla \left[B \left(1 - \frac{E_{\perp}^2}{B^2}\right)^{1/2} \right] \right), \end{aligned} \quad (15)$$

$$\frac{d(m_0 \gamma^{*2} v_{\perp}^{*2} / 2B^*)}{dt} = \frac{d\mu_r^*}{dt} = 0. \quad (16)$$

Here, $\hat{\mathbf{b}}$ is the unit vector in the direction of the magnetic field, E , which can be split as $E = \sqrt{E_{\perp}^2 + E_{\parallel}^2}$, the amplitude of the electric field vector and v_{\parallel} the component of the particle velocity vector parallel to $\hat{\mathbf{b}}$. The drift velocity, perpendicular to \mathbf{B} is written as $\mathbf{u}_{\mathbf{E}} = \frac{c \mathbf{E} \times \hat{\mathbf{b}}}{B}$ and v_{\perp}^* is the perpendicular velocity the particle has, in the frame of reference moving at $\mathbf{u}_{\mathbf{E}}$. The magnetic field in that frame is given by $B^* = B(1 - E_{\perp}^2/B^2)^{1/2}$ up to first order. The relativistic magnetic moment μ_r^* is proportional to the flux through the gyration circle, again in the frame of reference moving at $\mathbf{u}_{\mathbf{E}}$, and this is constant. The Lorentz

factor is not constant, but oscillates at the gyrofrequency. This oscillation is averaged out as well, to give $\gamma = \gamma^*(1 - E_\perp^2/B^2)^{-1/2}$. Because of the appearance of the denominator $1 - E_\perp^2/B^2$ in the guiding centre equations of motion, it is evident that the perpendicular electric field E_\perp has to be smaller than B for the equations not to reach an unphysical singularity. The fourth equation following from this analysis describes the average rate of increase of the particles energy, which does not give more information up to first order, after applying the assumption of slowly varying fields and is therefore not evolved.

If the particle velocity is restricted to $v^2 \ll c^2$ and the magnitude of its drift velocity $u_E^2 \ll c^2$ then $\gamma \rightarrow 1$ and $1/\sqrt{(1 - E_\perp^2/B^2)} = 1/\sqrt{1 - u_E^2/c^2} \rightarrow 1$. Then also the relativistic magnetic moment, a constant of motion, becomes the classical magnetic moment $\mu_r = \frac{m_0 \gamma^2 v_\perp^2}{2B} \rightarrow \mu = \frac{mv_\perp^2}{2B}$. The additional, purely relativistic term on the right-hand-side of equation (14) is of the order v^2/c^2 compared to the other terms and hence, negligible in the Newtonian limit $v^2 \ll c^2$ (Northrop 1963). The Newtonian equations of motion for the guiding centre are then retrieved as

$$\frac{d\mathbf{R}}{dt} = v_\parallel \hat{\mathbf{b}} + \frac{\hat{\mathbf{b}}}{B} \times \left\{ -c\mathbf{E} + \frac{cm}{q} \left(v_\parallel \frac{d\hat{\mathbf{b}}}{dt} + \frac{d\mathbf{u}_E}{dt} \right) + \frac{\mu c}{q} \nabla B \right\}, \quad (17)$$

$$\frac{d(mv_\parallel)}{dt} = m\mathbf{u}_E \cdot \frac{d\hat{\mathbf{b}}}{dt} + qE_\parallel - \mu \hat{\mathbf{b}} \cdot \nabla B. \quad (18)$$

Comparing the relativistic guiding centre equations (14) to their Newtonian limit (17) shows how the separate drift terms are modified for relativistic particles of mass $m_0\gamma$. The first term on the right-hand-side of (14) is the motion parallel to $\hat{\mathbf{b}}$, unmodified because the factors of γ cancel. The second term (the first term in the cross product) is the $\mathbf{E} \times \mathbf{B}$ drift, which is also unmodified. The third term, combines the inertial drift (neglecting non-static fields, giving the curvature drift)

$$v_\parallel \frac{d\hat{\mathbf{b}}}{dt} = v_\parallel \frac{\partial \hat{\mathbf{b}}}{\partial t} + v_\parallel^2 (\hat{\mathbf{b}} \cdot \nabla) \hat{\mathbf{b}} + v_\parallel (\mathbf{u}_E \cdot \nabla) \hat{\mathbf{b}},$$

and the polarisation drift

$$\frac{d\mathbf{u}_E}{dt} = \frac{\partial \mathbf{u}_E}{\partial t} + v_\parallel (\hat{\mathbf{b}} \cdot \nabla) \mathbf{u}_E + (\mathbf{u}_E \cdot \nabla) \mathbf{u}_E,$$

where non-static fields are neglected. For these drifts the gyration period increases by a factor γ . Because the mass of the gyrating particle is γ times larger, the gyroradius is as well. Then, the magnitude of the magnetic field, in the frame of reference moving at \mathbf{u}_E , is $B^* = B(1 - E_\perp^2/B^2)^{1/2} = B\sqrt{1 - u_E^2/c^2}$ up to first order, explaining the factor $1/\sqrt{1 - u_E^2/c^2}$ appearing in all terms including the magnetic field magnitude. The ∇B drift, the fourth term, is also a factor γ larger than in equation (17) (a factor γ^2 is hidden in $\mu_r = m_0 \gamma^{*2} v_\perp^{*2}/2B^*$). The ∇B drift results from differences in the radius of curvature on opposite sides of the gyro-orbit, hence the larger the gyroradius, the larger the effect of the drift velocity. The last term on the right-hand-side of equation (14) is an additional,

purely relativistic drift in the direction $\hat{\mathbf{b}} \times \mathbf{u}_E$, which is the direction of E_\perp (Northrop 1963).

By comparing the equation of motion for the parallel momentum (15) to its Newtonian limit (18) it can be seen how the guiding center acceleration is modified for relativistic particles. The first term is the acceleration of a particle of mass $m_0\gamma$ due to a change of direction of \mathbf{B} . The parallel electric acceleration, the second term on the right-hand-side of (15), is unmodified relativistically since no mass is involved in that term. The third term in the parallel acceleration, the mirror deceleration is γ times larger in the relativistic equation (15). Again because the mass, and hence the gyroradius are larger by a factor γ .

Depending on the relative strength of the perpendicular electric field, the guiding centre equations for slowly varying fields (14)-(16) can be simplified further. If the perpendicular electric field is small compared to the other terms, the purely relativistic drift vanishes and the reference frame moving with \mathbf{u}_E becomes irrelevant. This is the set of equations used in recent work by Rosdahl and Galsgaard (2009), Gordovskyy et al. (2014) and Pinto et al. (2016) to analyse test particle acceleration in the solar corona. We will quantify the importance and relevance of all separate drift terms and the parallel electric field in Section 5.

It should be noted that for strongly magnetised plasmas ($\sigma > 1$), which are thought to be ubiquitous around pulsars, magnetars or black holes, the aforementioned assumptions break down. The relativistic global flow in this case has an Alfvén velocity close to the speed of light and the temporal variations of the fields are on the same scale as the temporal variations of the particles. The typical Lorentz factors particles in relativistic global flows around compact objects can reach also causes a particle gyration radius (13) too large for the guiding centre approximation to be valid. The MPI-AMRVAC code has the option to solve the full equation of motion (12) in relativistic plasma environments (Porth et al. 2016). This option can also be used as an accuracy test of the guiding centre approximation (GCA).

The GCA calculations have been performed using a fourth order Runge-Kutta scheme with adaptive time stepping. The typical timestep for the evolution of the guiding centre variables (the particle position in three-space, its relativistic momentum and magnetic moment) is much smaller than the MHD timestep in the cases we explore. Therefore, the MHD fields are considered static on particle timescales, and it is possible to evolve particles dynamically in an MHD snapshot. The MHD data is dimensionless and is scaled to CGS units before being used in the test particle calculations.

The particle timestep δt is determined based on its parallel acceleration $a = dv_{\parallel}/dt$ and velocity $v = \sqrt{(v_{\parallel})^2 + (v_{\perp})^2}$ as the minimum of $\delta r/v$ and v/a , where δr is the grid step restricted by the particles cfl condition of 0.8 making sure a particle cannot cross more than one cell of the MHD grid. Then an Euler integration step is taken with this timestep, to predict the particles trajectory. Based on the results of this Euler integration a definitive timestep for the Runge-Kutta integration is chosen as the minimum of the Euler timestep used and the new timesteps determined by the new acceleration, velocity and position as $(v/a)_{Euler}$ and $(\delta r/v)_{Euler}$.

The electric and magnetic fields and their spatial derivatives, for the right-hand-side of equations (14)-(16), are taken from the resistive MHD simulations by linear interpolation for each particle position, within four-dimensional cells

(x, y, z, t) from the adjacent grid points. The interpolations in space and time are performed between the CFL limited MHD steps. However, in this work we are advancing particles in static MHD snapshots without advancing the MHD fields. The separate drift terms in the right-hand-side of equation (14) are also interpolated and their absolute values are computed at every timestep to analyse which mechanism accelerates individual particles. The particles Larmor radius $R_L = \frac{\gamma m_0 v_\perp}{Bq}$ is also calculated at every timestep and compared to the typical cell size to validate the usage of the guiding centre approximation. The velocity v_\perp corresponds to all terms of equation (14) perpendicular to the magnetic field. For a Maxwellian velocity distribution with $v = \sqrt{(v_\parallel)^2 + (v_\perp)^2}$, the thermal velocity is $v_{th} = \sqrt{(2k_B T / m_p \frac{\rho_0}{\rho_0})} \sim 10^7 m/s$ for protons in a fluid of temperature about $T = 10^6 K$ with the proton rest mass $m_p = 1.6726 \cdot 10^{-24} g$ and dimensionless pressure p_0 and fluid density ρ_0 as defined in Section 2.1. In typical astrophysical low- β plasmas like the solar corona, for particles with thermal velocity and a typical magnetic field of $10^{-2} T$ the Larmor radius is of the order $R_L \sim 10^{-3} m$. Typical cell sizes for the highest effective resolution of 4800^2 are of the order $10^4 m$. So even in more extreme circumstances, if the particles are accelerated to non-thermal velocities, the Larmor radius may increase up to 7 orders until the guiding centre approximation fails. The magnetic moment is initially determined as $\mu_r^* = m_0 \gamma^{*2} v_\perp^{*2} / 2B^*$, where the velocity perpendicular to the magnetic field v_\perp^* , in the frame of reference moving at \mathbf{u}_E , corresponds to the gyration velocity v_g . The particles Lorentz factor is $\gamma = 1 / \sqrt{1 - v^2/c^2}$.

At all four x and y boundaries we employ open boundaries. Particles are allowed to leave the physical domain and are then destroyed. In 3D setups the boundaries in the z -direction are periodic, in accordance with the MHD boundary conditions. In 2.5D the third direction is invariant for MHD quantities, meaning that there is no boundary for particles to travel in the z -direction in our setups. This can cause the particles to accelerate indefinitely in the parallel, resistive electric fields and in the current channels (up to the speed of light).

The magnetic moment μ_r^* of each particle is conserved (16). Therefore we can distinguish between particles accelerated by a parallel electric field and particles accelerated by the drift terms in equation (14). A particle accelerated by a parallel electric field $E_\parallel = \eta J_\parallel$, has a relatively small pitch angle $\alpha = \arctan(v_\perp^* / v_\parallel)$. Whereas a particle accelerated by the drift terms has a relatively large pitch angle. The perpendicular velocity v_\perp^* in the frame of reference moving at velocity \mathbf{u}_E is determined by equation (16).

3 Results in 2.5D configurations

The ideal MHD equilibrium, either in a force-free or a non-force-free description is subject to an instability in which the current channels repel one another. In 2.5D, where the dynamics in the z -direction are invariant, this linear instability consists of an antiparallel displacement of each of the current channels along the y -direction (the two channels are initially located left and right from $x = 0$). After this displacement the channels undergo a rotation and a twisting motion. Based on an energy principle one can show that analytically, the combination of displacement and rotation drives instability (Richard et al. 1990). The growth rate of this instability is typically quantified by a linear growth phase in the

bulk kinetic energy (Keppens et al. 2014). During the linear and the subsequent nonlinear phase of the instability, magnetic field lines can reconnect with the background magnetic field. Reconnection of magnetic field lines causes nearly-singular current sheets and secondary islands to form in which particles can get accelerated.

3.1 General features, energy conversion, resistivity and reconnection

To analyse the growth rate of the tilt instability, we quantify the bulk kinetic energy in the displacing current channels. We use tracers to identify the current channels after they have started their displacement and to quantify energy measures.

Fig. 1 shows the evolution of a mean value as in (11) for a kinetic energy density $f = 0.5\rho u^2$ for all equilibrium configurations. We compare the growth rates of the tilt instability in the different setups, quantified by a linear fitting routine. Half the slope of the linear fit of the kinetic energy in logscale sets the growth rate γ_{tilt} (mentioned in Table 1 for all runs with effective resolution 2400×2400). For force-free cases the growth rate increases with decreasing plasma- β , from cases F2dff to K2dff, namely, $\gamma_{\text{tilt}}^F = 1.6578$, $\gamma_{\text{tilt}}^G = 1.6510$, $\gamma_{\text{tilt}}^H = 1.6492$, $\gamma_{\text{tilt}}^I = 1.5793$, $\gamma_{\text{tilt}}^J = 1.4968$ and $\gamma_{\text{tilt}}^K = 1.4018$. This is in accordance with the (low-resolution) results of Richard et al. (1990). Whereas for the non-force-free cases we find the opposite trend, decreasing growth rate with decreasing plasma β , with all values agreeing with the ones reported in Keppens et al. (2014). We have verified that this growth rate estimate does not change when using the other current channel or when using the entire domain to calculate the mean kinetic energy. Compared to the non-force-free setup from Keppens et al. (2014), the perfect linear growth phase in kinetic energy is generally shorter, spanning the time interval $t \in [4.5, 5.5]$ for the force-free configurations, compared to $t \in [3, 7]$ for the non-force-free configurations. It also starts later, ends earlier and yields a faster evolution, confirming the early findings of Richard et al. (1990) for a force-free equilibrium with low plasma- β . It is interesting to note differences in the relation of the growth rate with plasma- β for the different setups. The force-free setup gives us the opportunity to reach a plasma- β which is three times smaller than in the non-force-free cases explored by Keppens et al. (2014). In Fig. 1 we also show the evolution of the kinetic energy for cases F2dffAR and G2dffAR with anomalous resistivity rather than uniform resistivity. Both cases have the exact same settings as F2dff and G2dff, except for the resistivity only being nonzero in regions with current density $j > j_c = 12$ with j_c chosen to be larger than the peak current at equilibrium. The onset of the tilt instability in these cases starts at earlier time compared to F2dff and G2dff and lasts for a longer period. The slope of the linear growth phase of the tilt instability is steeper than for their respective uniform resistivity equivalents, $\gamma_{\text{tilt}}^{FAR} = 1.8206$ and $\gamma_{\text{tilt}}^{GAR} = 1.8012$, and for a case with the anomalous resistivity threshold $j_c = 500 > \max(J_z(t = 0))$ and hence, just numerical resistivity, $\gamma_{\text{tilt}}^{FAR2} = 1.6404$. The peak value of the kinetic energy that is reached is the same as in the cases with uniform resistivity, such that the tilt instability has a longer time to grow, with a larger growth rate, to develop strong current sheets.

Fig. 2 shows the evolution of (11) for a kinetic energy density $f = 0.5\rho u^2$, magnetic energy density $0.5B^2$, internal energy density $p/(\Gamma - 1)$ and an Ohmic

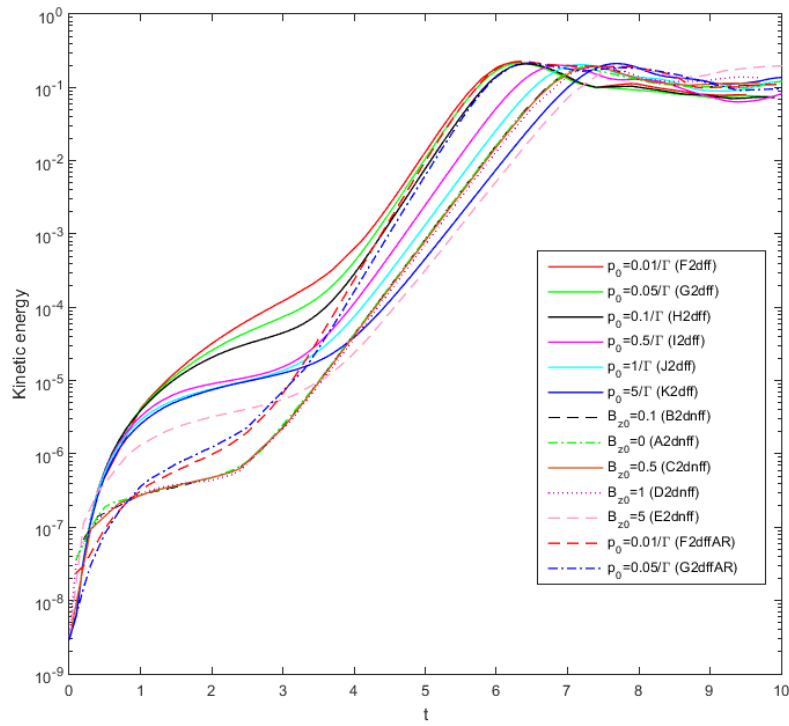


Figure 1: Kinetic energy density evolution for all 2.5D runs with effective resolution 2400^2 (except F2dffAR2), at all times integrated over a single current channel as identified by an advected tracer, distinguished by line style and colour.

heating term ηJ^2 (which is really an energy density rate change). Two curves are shown for each quantity, one with effective resolution 4800×4800 and one with effective resolution 2400×2400 , for the force-free case with initial pressure $p_0 = 0.05/\Gamma$, to demonstrate convergence. A third curve is shown for each quantity, for the same case with effective resolution 2400×2400 , with an anomalous resistivity model applied. Judging on these global energetic indicators, the results are nicely converged, with minor differences only in the far nonlinear regime of the evolution for the cases with uniform resistivity and only differing in resolution. The case shown has magnetic energy dominating internal energy (due to $\beta < 1$ conditions). The magnetic energy also clearly dominates the kinetic energy. The internal energy grows in the interval $t \in [0, 6]$, which can be explained by the low β conditions. Due to low pressure, relative to the magnetic pressure, the work done by the strong magnetic field, compresses the plasma. The rise in internal energy is more significant (and visible on a log scale) in the low β regime due to the low initial pressure, while the magnetic field configuration is the same in all force-free cases. The Ohmic heating also shows a transition around $t \approx 5$, lagging the growth phase of the kinetic energy.

Using an anomalous resistivity model, rather than uniform resistivity, has an effect on the energetics. For a critical current density $j_c = 12$, larger than the largest value of the current in equilibrium, the effects on kinetic energy and Ohmic heating are clearly visible in Fig. 2 for case G2dffAR. The onset of the linear growth of the kinetic energy (red line with asterisks as a marker) starts earlier and lasts longer. This means that the instability has a longer time to grow and that larger current density can be reached during the linear growth. The integrated ohmic heating starts at a lower value, because the lack of resistivity in regions with a current density $j < j_c$. Because the linear growth phase lasts longer, the ohmic heating can build up for a longer time and it reaches almost the same value in the nonlinear phase as the case with uniform resistivity. The magnetic energy and the internal energy show less to no effect due to anomalous resistivity.

Near-singular current sheets are formed at the boundaries of the rotating islands where antiparallel field lines can reconnect, causing this heating of the plasma. In all non-force-free cases a linear growth phase of the logarithm of the peak current density is established, in accordance with results for force-free configurations in Keppens et al. (2014). The linear growth for $\log(\max(J_z))$ is accurately resolved with our block-AMR strategy in combination with our third-order spatio-temporal treatment, showing up to secondary tearing-type instabilities. In Fig. 3, the evolution of the peak current $\log(\max(J_z))$ is shown in a log-linear scale for all force-free 2.5D cases, the non-force-free case with $B_{z0} = 0.1$ is shown for comparison. For the force-free case with $p_0 = 0.01/\Gamma$ we show all three resolutions (f2dff, F2dff, FF2dff) to show a local measure of convergence. In the island-dominated phase, beyond $t \approx 6$ for the non-force-free case with the fastest kinetic energy density evolution (F2dff), there are still noticeable differences for the highest resolutions. The low resolution run (f2dff) reaches much lower peak current values than the two high resolution runs. Comparing runs at identical resolutions of 2400^2 , we can detect a trend of the current evolution for different β . For the force-free equilibrium there is a systematic delay in the onset of the singular current development when raising β (which corresponds to raising the initial pressure p_0 in the force-free cases). This is opposite of what Keppens et al. (2014) found for non-force-free equilibria

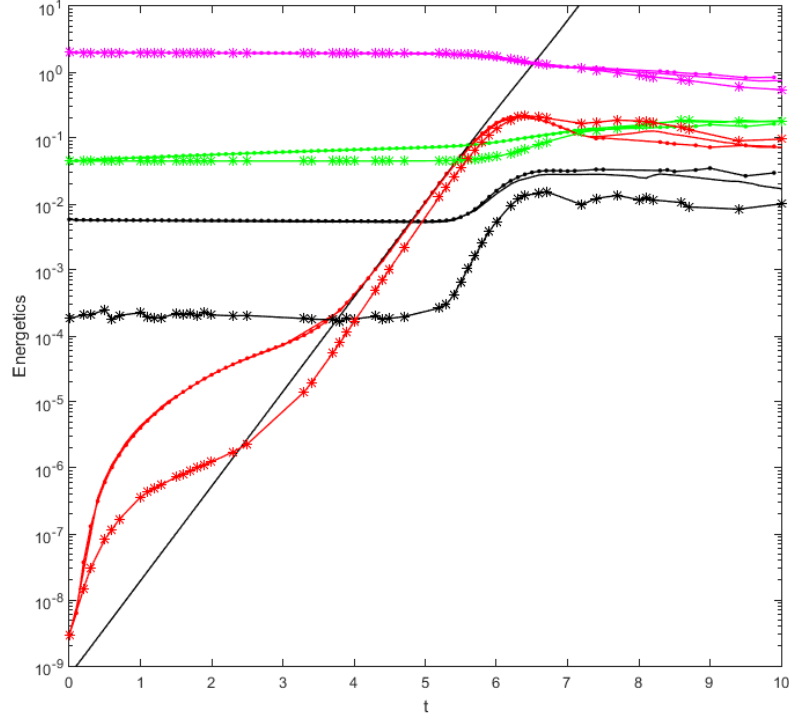


Figure 2: The evolution of kinetic (red), magnetic (magenta) and internal energy (green) density, at all times integrated over a single current channel as identified by an advected tracer, for 2.5D force-free case with $p_0 = 0.05/\Gamma$ (G2dff, GG2dff and G2dffAR). Each curve is shown at two resolutions (2400^2 with a solid line and 4800^2 with dots as indicators) and for a run with anomalous resistivity applied (2400^2 , with asterisks as indicators). The Ohmic heating effect is quantified by the black curve. The straight thin black line is a fit to the linear growth in kinetic energy.

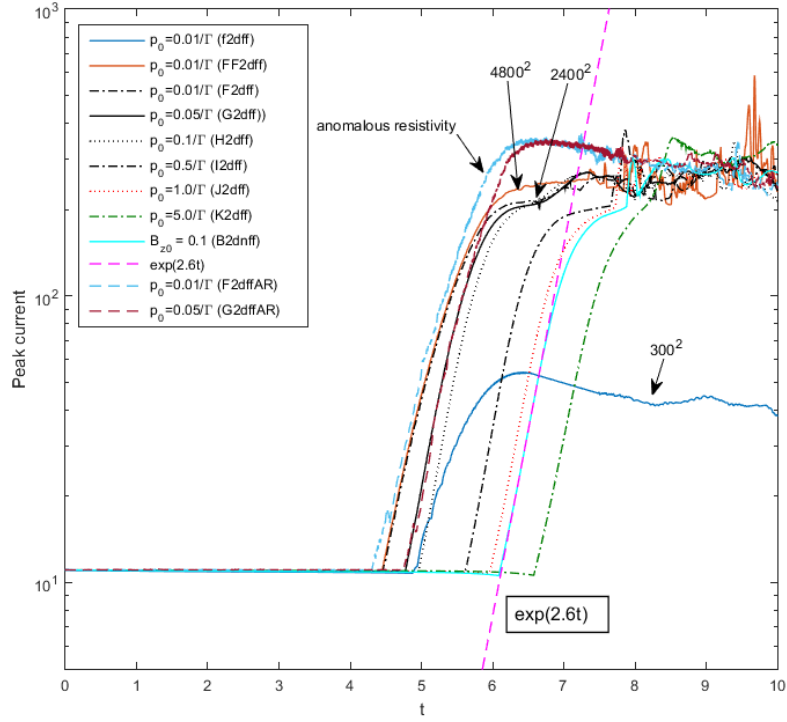


Figure 3: Peak current evolution for all force-free 2.5D runs, distinguished by line style and colour. Non-force-free run B2dnff ($B_{z0} = 0.1$) is shown as a comparison. Different resolutions are shown for force-free case with $p_0 = 0.01/\Gamma$. Runs with anomalous resistivity are shown for force-free cases with $p_0 = 0.01/\Gamma$ and $p_0 = 0.05/\Gamma$. Exponential growth at $\exp(2.6t)$ is indicated to guide the eye.

(delay when lowering β), but agrees with the findings of Richard et al. (1990) for their low-resolution force-free runs. For comparison, $\log(\max(J_z))$ for the non-force-free cases with fastest evolution is plotted as well in Fig. 3. This case shows a slower evolution of the peak current than all force-free cases except case K2dff, with highest initial pressure $p_0 = 5.0/\Gamma$ and $\tilde{\beta} = 18.1$. All cases, both force-free and non-force-free, roughly have the same slope for the onset of this singularity, indicated by $\log(\max(J_z)) \sim 2.6t$ (plotted by the dashed, magenta line). The systematic delay observed is consistent with the tilt mode growth rates, which are quantified by the linear growth phase of the kinetic energy in Fig. 1.

Given the ideal character of the tilt instability, there is hardly any effect of (anomalous) resistivity on the peak current during the phase before the linear tilt growth. The evolution of the peak current (Fig. 3) for cases with anomalous resistivity is similar to the cases with uniform resistivity. However, during the linear growth phase, the growing gradient of the magnetic field causes the current to grow in specific areas. In these areas resistivity is switched on, but in the surroundings, resistivity is still zero. This means that the current cannot diffuse into the surroundings and it will build up for a longer time. In the setups with anomalous resistivity therefore, a higher peak current is reached and the linear growth phase lasts longer. Due to this effect, there are also visual differences in the total current density. In the models with anomalous resistivity, secondary islands and narrow current sheets grow earlier in the simulation and do not diffuse into the surroundings. As long as the threshold for anomalous resistivity to be nonzero is larger than the peak current value at equilibrium ($j_c > 11$), there are no differences in the peak currents reached during the nonlinear phase, nor are there any visual differences in the topology of the current distribution. However, there is no parallel electric field component $E_{\parallel} = \eta \mathbf{J} \cdot \mathbf{b}$ anymore in the regions with a low current density. This has an expected effect on particle acceleration in the ambient and inside the current channels, but not at reconnection sites with a large peak current density. The behaviour for different plasma- β (at equilibrium) does not change. The same peak current is reached for all force-free cases with anomalous resistivity and in the nonlinear phase there are minor differences just as for the cases for uniform resistivity.

The plasma β dependence of the linear tilt mode growth rate for force-free configurations is stronger than the weak dependence found for non-force-free setups. Which can be concluded both from the calculated γ_{tilt} or from the delay in both the linear growth rate of kinetic energy density (Fig. 1) and the increase in the peak current (Fig. 3) for increasing plasma β for the force-free cases. For the non-force-free setup all cases show a weaker plasma β dependence for the linear tilt mode growth rate, but all cases show the singular current growth after which they saturate in a similar manner. Peak currents of a factor of 30 above the initial peak current value are reached, up to values of order $\mathcal{O}(300)$. The overall evolution for all cases is similar, however the force-free cases with plasma $\beta < 1$ show faster development of nearly singular current sheets and secondary islands on the current sheets. Fig. 4 shows the total current magnitude J for three force-free cases (F2dff, F2dffAR with anomalous resistivity applied and J2dff) next to each other at times $t = 6, 7, 8$ and 9 and again, the 2.5D non-force-free case with the fastest peak current evolution (B2dnff) as comparison. A linear colour scale (with values between 0-50) is used for all frames, such that all structure is visible. Cases B2dnff and J2dff, both with plasma $\beta > 1$,

show a very similar evolution, as is also indicated by their tilt mode growth rate $\gamma_{ilt}^B \approx \gamma_{ilt}^J \approx 1.497$. They reach the disruption of the current sheets by tearing-type chaotic reconnection beyond $t = 9$, whereas the other force-free cases shown, with a plasma $\beta < 1$, show this turbulent stage already at $t = 8$. The chaotic formation of secondary islands on the disrupting current sheets can also be seen in Fig. 4 at $t = 8$ for cases F2dff and F2dffAR and at $t = 9$ for case J2dff and non-force-free case B2dnff. Cases F2dff and F2dffAR only differ in the resistivity model applied. Case F2dffAR shows a similar evolution of the current up to $t = 7$, but hereafter the current diffuses in a different manner due to the anomalous resistivity model.

Besides the different equilibrium setups, the dynamics are affected by differences in initial conditions (pressure for force-free setups and perpendicular magnetic field component for non-force-free setups), hence different plasma β . This leads to differences in where secondary islands appear and how they deform. And hence, also where reconnection occurs exactly. To analyse where particles will get accelerated most efficiently, we locate reconnection sites based on several indicators. Reconnection regions in this essentially 2D system can be identified by a non-zero electric field, parallel to the magnetic field, E_{\parallel} , indicated by a parallel current density, i.e., $E_{\parallel} = \mathbf{E} \cdot \mathbf{B}/B = \eta \mathbf{J} \cdot \mathbf{B}/B \neq 0$ (Priest and Forbes 2000). A region of non-zero parallel electric field is strongly suggesting reconnection. However, mathematically, a more stringent, formal criterion for reconnection can be written as (Biskamp 2000; Lapenta et al. 2015)

$$|\hat{\mathbf{b}} \times (\nabla \times E_{\parallel} \hat{\mathbf{b}})| \neq 0 \quad (19)$$

normalised by $B = |\mathbf{B}|$, the magnitude of the magnetic field. This is a direct measure of the violation of conservation of frozen-in magnetic field lines, indicating reconnection. This measures the rotation of the magnetic field lines, induced by the parallel electric field.

The most direct evidence is obtained by finding field lines that started in the direction from top to bottom in (y), but have reconnected and changed topology. We show the parallel electric field including selected magnetic field lines at $t = 0$ in Fig. 5 to compare the topology at equilibrium and in the nonlinear phase. Selected magnetic field lines are plotted on top of the reconnection indicators $E_{\parallel} \neq 0$ and equation (19) in Fig. 6 and Fig. 8 respectively, for force-free case F2dff with uniform resistivity and in Fig. 7 and Fig. 9 for F2dffAR with anomalous resistivity. For case F2dff, there is only positive parallel electric field inside the current channels initially and no reconnecting field lines, nor $|\hat{\mathbf{b}} \times (\nabla \times E_{\parallel} \hat{\mathbf{b}})| \neq 0$ at $t = 0$. For F2dffAR there is no parallel electric field in the equilibrium phase due to a lack of resistivity.

At $t = 8$, negative parallel electric field has developed at the boundaries of the tilted current channels and in between for both cases. This confirms that likely reconnection sites develop in the strong current layers and in between the current channels. Anti-parallel field lines break and reconnect in these regions and topological changes occur, including the formation of secondary islands. The global topological rearrangements establish field lines reconnecting between $x > 0$ (right of the initial current channels) and $x < 0$ (left of the initial current channels) regions. There is one major difference between cases with uniform resistivity and with anomalous resistivity, expected to have a major effect on

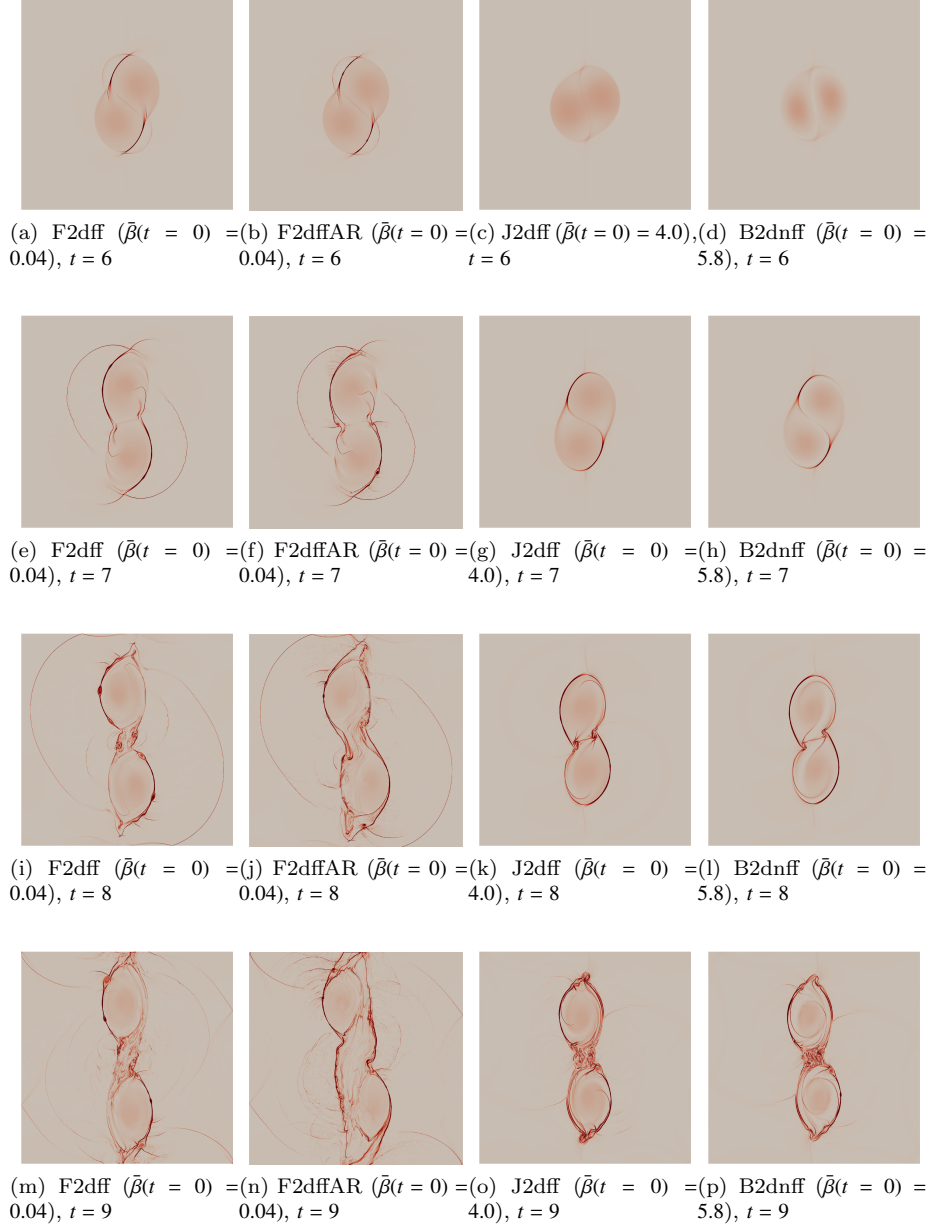


Figure 4: Evolution of the total current magnitude $|\mathbf{J}|$ for force-free cases F2dff, F2dffAR, J2dff (respectively, starting from left) and non-force-free case B2dnff (right). The four rows correspond to times $t = 6, 7, 8$ and 9 , respectively. A linear colour scale is saturated to show values between $[0 - 50]$, showing all of the structure.

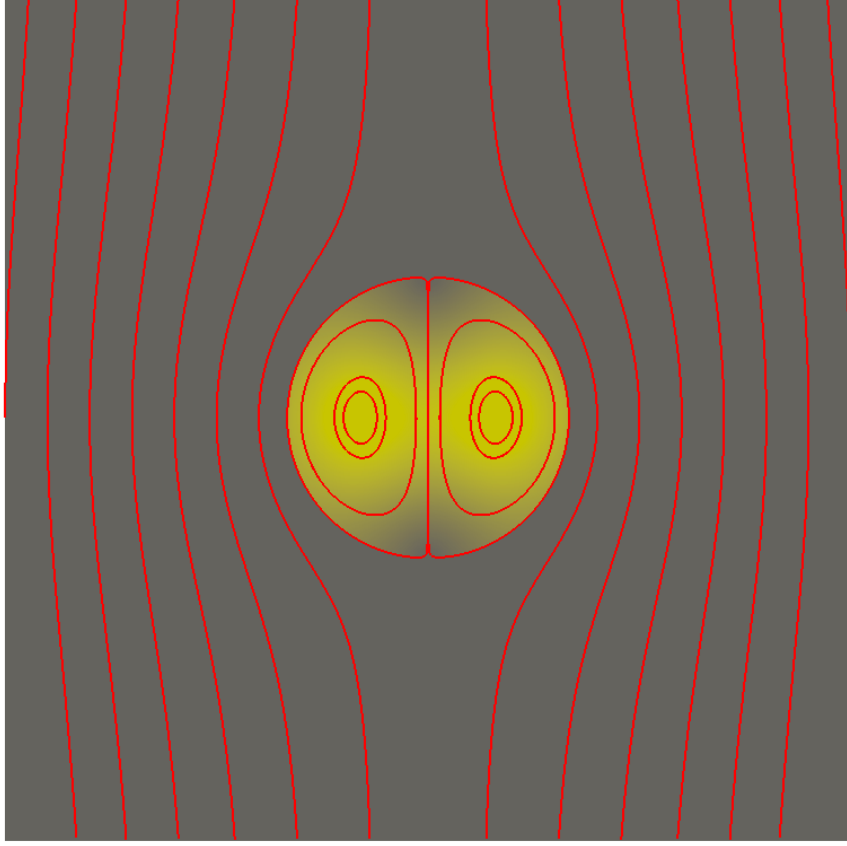


Figure 5: For all force-free cases, we show the parallel electric field $E_{\parallel} = \mathbf{E} \cdot \mathbf{B} / B$ at equilibrium ($t = 0$) and selected field lines (in red) indicating the magnetic field structure. A linear colour is saturated to show values between $[-0.001, 0.001]$.

particle acceleration. For case F2dff, in Fig. 6, there is a strong parallel electric field inside the current channels whereas for F2dffAR, in Fig. 7, there is no parallel electric field inside the current channels. The location of strongest violation of field line topological connectivity as indicated by equation (19), in Fig. 8, coincides with the reconnection regions identified by the non-zero parallel electric field. However, one should be careful judging the occurrence of reconnection based on the presence of parallel electric field, as is clear from the equilibrium F2dff shown in Fig. 5 and from the nonzero parallel electric field inside the current channels in Fig. 6. In the reconnection regions as indicated by equation (19), there is however a strong parallel electric field in both cases F2dff and F2dffAR. These differences due to resistivity are expected to have a large effect on particle acceleration due to parallel electric field in the regions where no reconnection occurs. Similar observations hold for all force-free and non-force-free cases, with differences in the exact topology of the magnetic field and the time the reconnection develops.

After identifying and locating strong reconnection sites it is interesting to analyse by which mechanisms particles are accelerated in these regions. This is

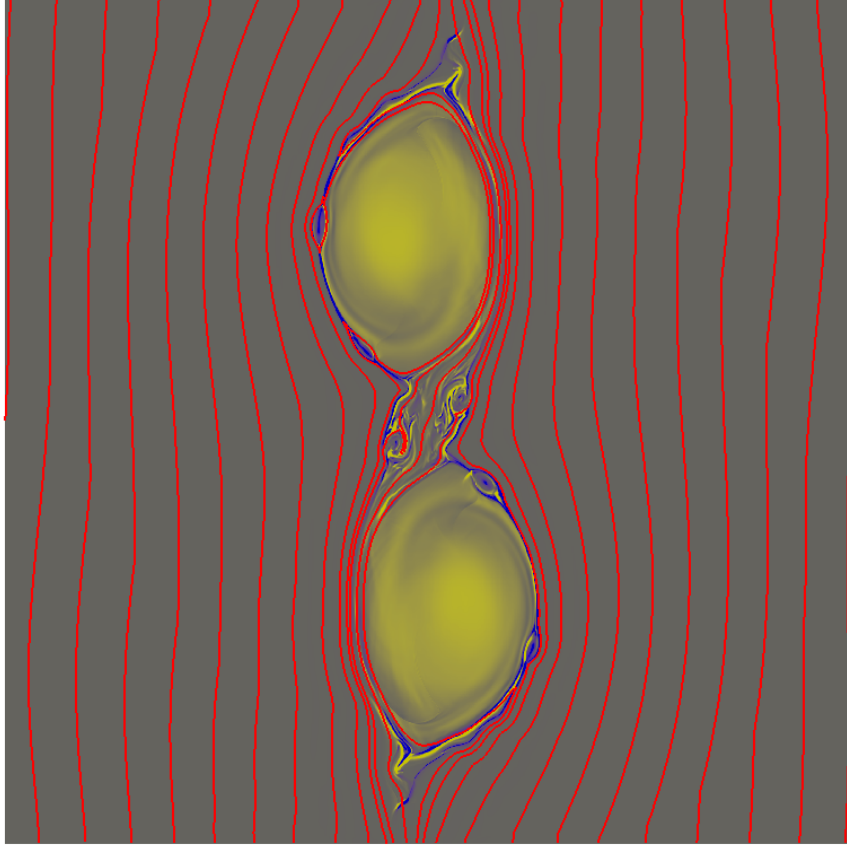


Figure 6: For force-free cases F2dff ($\bar{\beta}(t = 0) = 0.04$ and $p_0 = 0.01/\Gamma$), we show the parallel electric field $E_{\parallel} = \mathbf{E} \cdot \mathbf{B}/B$ at $t = 8$ and selected field lines (in red) indicating the magnetic field structure. A linear colour is saturated to show values between $[-0.001, 0.001]$.

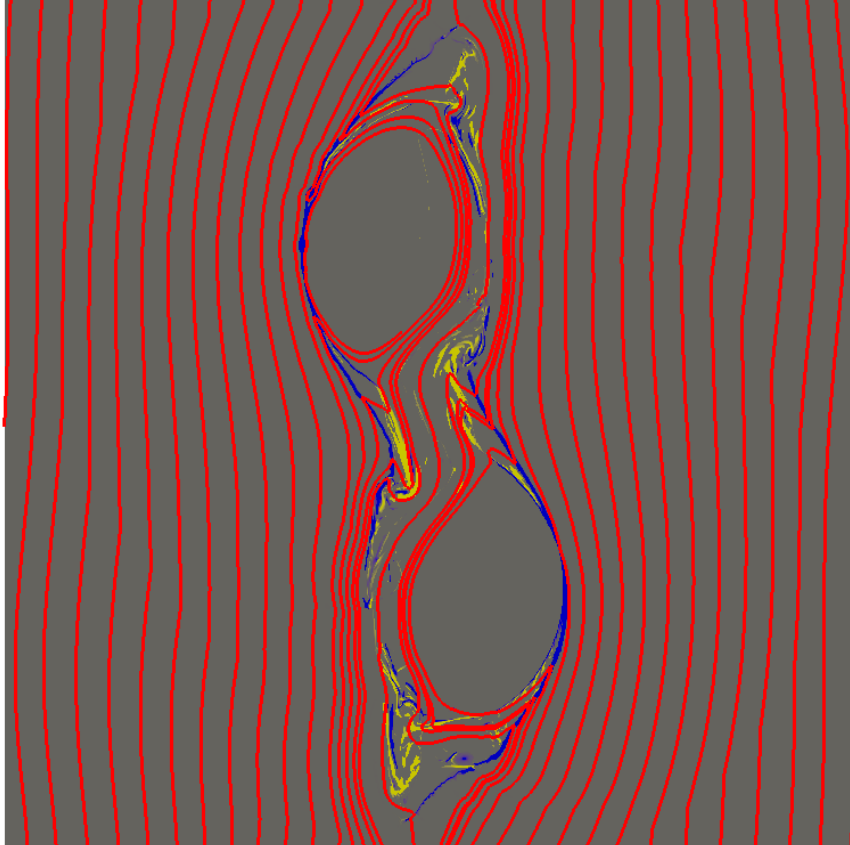


Figure 7: For force-free cases F2dffAR ($\bar{\beta}(t = 0) = 0.04$ and $p_0 = 0.01/\Gamma$), we show the parallel electric field $E_{\parallel} = \mathbf{E} \cdot \mathbf{B}/B$ at $t = 8$ and selected field lines (in red) indicating the magnetic field structure. A linear colour is saturated to show values between $[-0.001, 0.001]$.

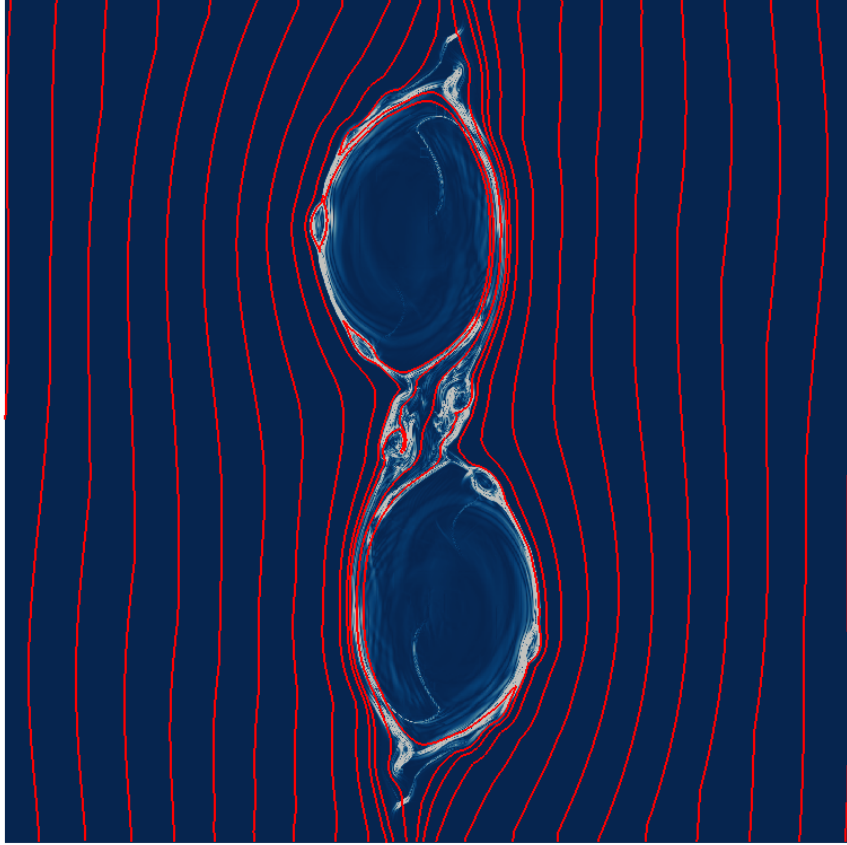


Figure 8: For force-free cases F2dff ($\bar{\beta}(t=0) = 0.04$ and $p_0 = 0.01/\Gamma$), we show the topological measure of field line breakage, normalised by the magnetic field magnitude B : $|\hat{\mathbf{b}} \times (\nabla \times E_{\parallel} \hat{\mathbf{b}})|$ at $t = 8$. Selected magnetic field lines (in red) are shown, indicating the magnetic field structure. A linear colour is saturated to show values between $[0, 0.05]$.

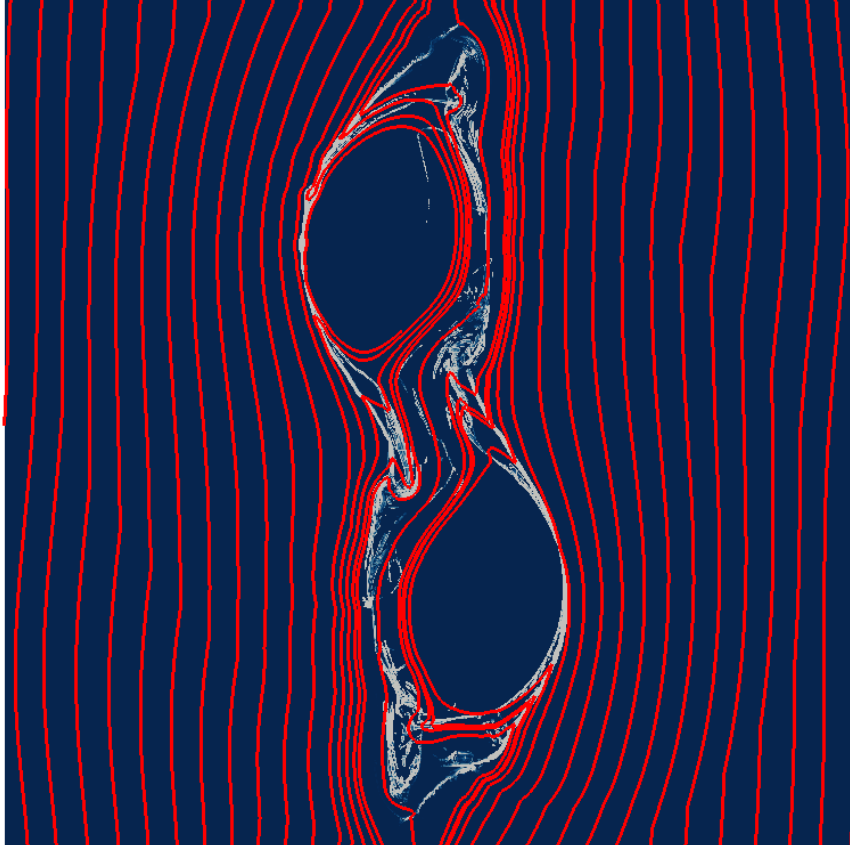


Figure 9: For force-free cases F2dffAR ($\bar{\beta}(t = 0) = 0.04$ and $p_0 = 0.01/\Gamma$), we show the topological measure of field line breakage, normalised by the magnetic field magnitude B : $|\hat{\mathbf{b}} \times (\nabla \times E_{\parallel} \hat{\mathbf{b}})|$ at $t = 8$. Selected magnetic field lines (in red) are shown, indicating the magnetic field structure. A linear colour is saturated to show values between $[0, 0.05]$.

done in Section 5.

4 Results in 3D configurations

In 2.5D configurations minor differences are observed for varying plasma- β . The role of the vertical B_z component is similar for all force-free cases and for the non-force-free cases. (Keppens et al. 2014) showed that the role of B_z is minimal since the translational invariance prevents potential (de)stabilisation due to field line bending. In 3D scenarios the field lines may bend with respect to the z -direction. A second additional effect is the fact that each current channel may be liable to an ideal kink instability. From the Kruskal-Shafranov limit we know that for $K_{cr} \equiv |\bar{J}_z|/\bar{B}_z < 2a/R_0 = 4\pi a/L \approx 1$ the equilibrium is stable, where we use a plasma column radius $a \approx 0.5$ and length $L = 6$. We quantify the ratio $K_{cr} \equiv |\bar{J}_z|/\bar{B}_z$, from the initial condition for all cases (mentioned in Table 1 for all 3D runs) and we find that all force-free cases are liable to a kink instability since $K_{cr} = 3.83$. For the non-force-free setup, only the lowest plasma- β case, E2dnff, is stable, as was confirmed numerically by Keppens et al. (2014). For non-force-free cases B2dnff to E2dnff, we find, respectively, 43.5, 8.7, 4.35 and 0.87 for the Kruskal-Shafranov limit. Therefore we expect that all 3D cases, except E3dnff, will show kink unstable behaviour, since they have an insufficient vertical magnetic field B_z to stabilise kink deformations. This allows us to explore the low plasma- β regime without the limitation of strong vertical magnetic fields stabilising the equilibrium as is the case for non-force-free configurations. We will analyse what the result is of the kink instability in a force-free setup on magnetic reconnection.

4.1 Effect of the kink instability on energy conversion and reconnection

In Fig. 10 we show the evolution of the peak current for all force-free 3D runs (similar to Fig. 3, for the 2.5D cases). Non-force-free case B3dnff, with $B_{z0} = 0.1$, is also included for comparison. This case shows the fastest evolution of the peak current of all non-force-free setups and has the largest, finite, Kruskal-Shafranov limit $K_{cr} = 43.5$. The B_{z0} component is the same for all force-free cases, resulting in the same Kruskal-Shafranov limit. As the initial pressure p_0 increases, and hence plasma- β increases, the onset of the tilt instability is delayed. This is indicated by the delay in the onset of the near-singular peak current evolution. However, unlike in the non-force-free cases, where the setup with lowest plasma- β (E3dnff, with $B_{z0} = 5.0$) completely suppresses any instability development (Keppens et al. 2014), all force-free cases develop a combination of tilt and kink instabilities. In all 3D force-free cases, the onset is delayed by the magnetic tension due to the B_z component. And this effect is stronger, for higher pressure and plasma- β . If the initial velocity perturbation has no z dependence, the evolution of the 3D cases behaves identical to the 2.5D cases and the tilt instability develops at earlier time.

As expected from the Kruskal-Shafranov limit, the force-free setups all develop tilt-kink unstable behaviour. However, compared to the non-force-free runs, the instabilities are delayed. And in the cases with highest initial pressure and plasma- β the far nonlinear stage is not reached within the simulation time.

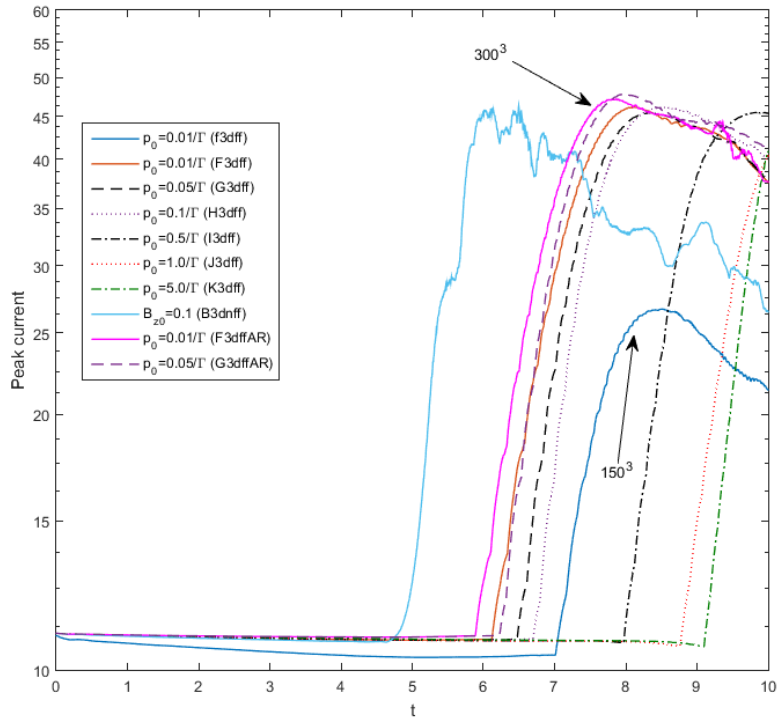


Figure 10: Peak current evolution for all force-free 3D runs, distinguished by line style and colour. Non-force-free run B3dnff ($B_{z0} = 0.1$) is shown as a comparison. Different resolutions are shown for the force-free case with $p_0 = 0.01/\Gamma$ (F3dff).



Figure 11: Total current, integrated along the line of sight, for case F3dff ($\bar{\beta}(t=0) = 0.04$) at $t = 8$. On the left, we integrate along z with a colour scale saturated to 60. In the middle, we integrate along x and on the right we integrate along y , both with a colour scale saturated to 20.

Another important feature to notice in Fig. 10 is the difference for two similar setups with varying resolution. For the force-free cases F3dff and f3dff, both with $p_0 = 0.01/\Gamma$ but with effective resolutions of 300^3 and 150^3 respectively, the peak current evolution for lower resolution is delayed. The saturation levels attained in the far nonlinear regime are higher for the higher-resolution runs. Based on the higher-resolution runs in 2.5D this was to be expected and Keppens et al. (2014) shows that at even higher resolutions, higher saturation levels are reached. However, visual data inspection and more global convergence measures confirm that at a resolution of 300^3 sufficient detail is captured.

In all 3D force-free cases peak current enhancement develops due to the tilt instability. All cases show an additional development of kink deformations and accompanying fine-structure developing in both current channels. Fig. 11 shows the total line-integrated current magnitude for force-free case F3dff. A contour representation of $\int_{-3}^{+3} j dx_i$, is shown for the top view (i.e. $x_i = z$) and the two lateral views ($x_i = x$ and $x_i = y$), from left to right. All frames are taken at $t = 8$, just when the saturated, nonlinear regime is reached. In the two lateral views, the kinking of the current channels is visible, although the helical structure is not as clearly visible as for non-force-free cases Keppens et al. (2014). The current channels repel each other and are displaced in the y direction, which can be seen from the z -integrated view. The observed patterns in the top view are in agreement with the results from 2.5D simulations in Fig. 4. All force-free cases evolve in a similar way, developing the same structure and field topology, delayed for larger values of plasma- β . In true 3D renderings of the total current density, the force-free cases are compared to the non-force-free evolution as described in Keppens et al. 2014. In Fig. 12 and Fig. 13, we show three-slices of the total current density at $t = 6$, at the onset of the tilt instability, $t = 8$ at the end of the linear growth phase and at $t = 9$ in the far non-linear regime, for the fastest force-free case F3dff and fastest non-force-free case B3dnff, respectively. A very different pattern is observed for both cases. The higher axial field component in the force-free case (left), and hence, the smaller Kruskal-Shafranov limit suppresses some, but not all of the secondary mushroom-like features as are seen in the non-force-free case (right). In the force-free cases, there is no z -component of the magnetic field in the ambient, outside the current channels. The diffusion of the current in the surroundings

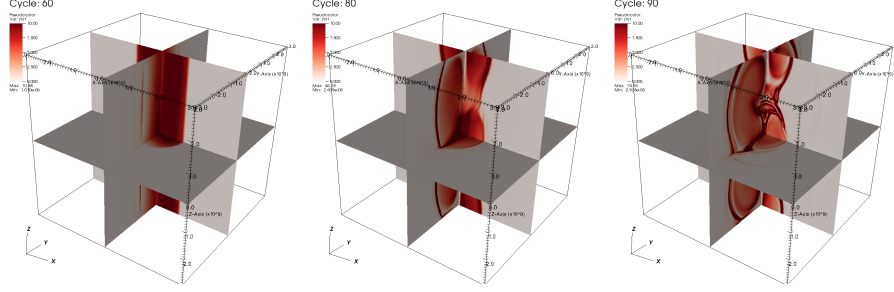


Figure 12: For the fastest force-free case F3dff as shown in Fig. 11 we show a 3D view of the total current density with slices cut through the three axes, at $t = 6$, $t = 8$ and $t = 9$ from left to right. The colour scale is saturated at $j = 10$. The box size is $6L \times 6L \times 6L$ with $L = 10^9 \text{cm}$.

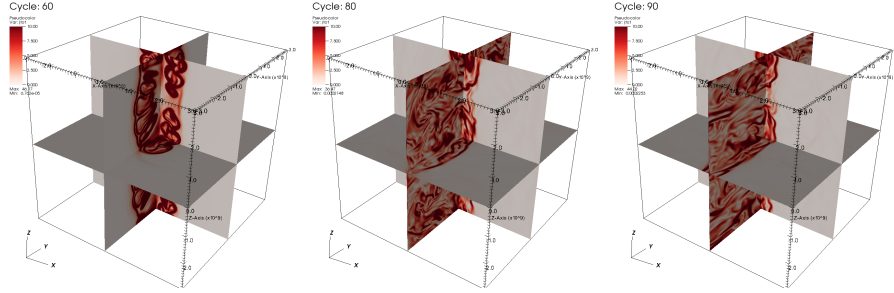


Figure 13: For the fastest non-force-free case B3dnff we show a 3D view of the total current density with slices cut through the three axes, at $t = 6$, $t = 8$ and $t = 9$ from left to right. The colour scale is saturated at $j = 10$. The box size is $6L \times 6L \times 6L$ with $L = 10^9 \text{cm}$.

of the current channels is therefore completely different from the non-force-free cases. Both cases demonstrate kinking behaviour, indicated by the helical deformations of the current channels. Both cases show development of thin sheet-like structures, indicated by a strong current.

The development of strong currents in these areas can also be seen in Fig. 14, for the same force-free case F3dff. Here we show the parallel, or resistive electric field on the same slices as in Fig. 12 and, with selected magnetic field lines, coloured by total current density, at the same times $t = 6$, $t = 8$ and $t = 9$ as Fig. 12.

Based on 2.5D results, the presence of parallel, resistive electric field is not the most accurate measure of reconnection occurring. Therefore we show a volume rendering of the change of topology of the magnetic field as measured by equation (19) in Fig. 15. From the top view on the right it is clear that the whole area of the current channels, including the boundaries and the area in between the channels is a reconnection site. From the side view on the left, the kinking of the current channels is visible and it shows that the reconnection region stretches all the way along the current channel in the z -direction.

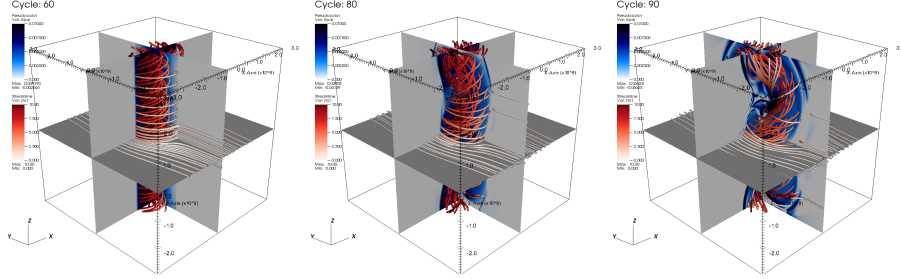


Figure 14: For the same force-free case F3dff as in Fig. 12 we show a 3D view of the parallel, resistive electric field E_{\parallel} with slices cut through the three axes, at $t = 6$, $t = 8$ and $t = 9$ from left to right. The colour scale is saturated at 0.001. Selected field lines are shown, coloured by their total current density value, saturated at $j = 10$. The box size is $6L \times 6L \times 6L$ with $L = 10^9 \text{ cm}$.

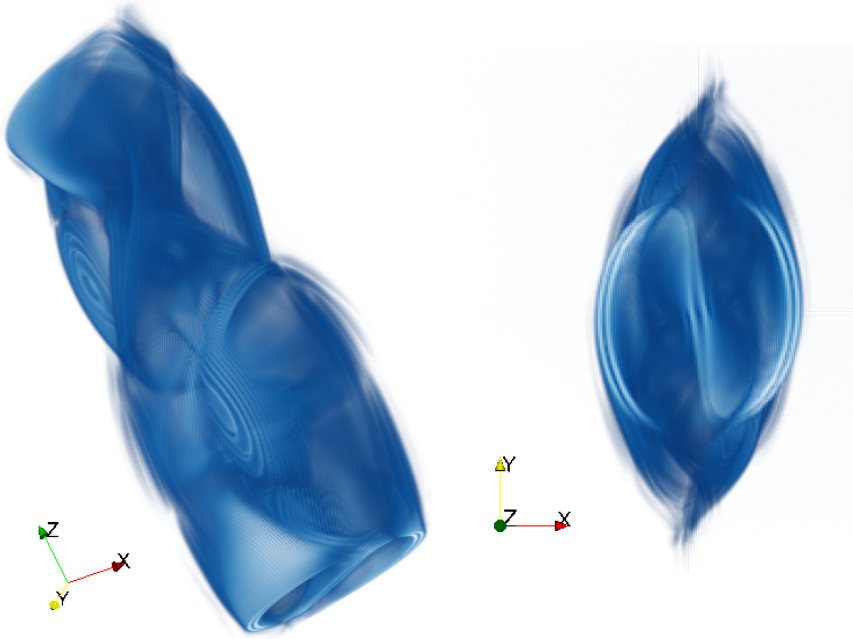


Figure 15: Same case as shown in Fig. 14, at $t = 8$. Shown is a volume rendering of the change of topology of the magnetic field according to equation (19), saturated at 0.05, in a side view on the left and a top view on the right.

5 Test particle acceleration

To analyse particle dynamics we solve the guiding centre equations of motion (14-16) for 200.000 test particles, to get the particles position, velocity and magnetic moment. Particles are initialised randomly over the domain in the $x - y$ plane, with a fraction of 0.99 of the ensemble uniformly distributed in space in a rectangular block, encapsulating the two (displaced) current channels and the areas with the largest current density, $x \in [-1, 1]$, $y \in [-3, 3]$. The other fraction of 0.01 of the ensemble is uniformly distributed over the full domain $x \in [-3, 3]$, $y \in [-3, 3]$, including the surrounding background. This way, most of the particles are in the physically interesting region around the current channels and for a resolution of 2400^2 and 200.000 particles we have an average density of more than one particle per cell. In the z -direction, which is invariant in the 2.5D simulations, particles are randomly and uniformly distributed in $z \in [-3, 3]$. Typical simulation box lengths are of the order $O(10^7 m)$, meaning that with an effective grid resolution of 2400^2 , the orbiting motion takes place on approximately 10^{-3} of a grid cell, for protons and for electrons even a factor 1800 smaller. The magnetic field as seen by a particle in orbit, will be constant across the gyro-orbit, if the magnetic field is obtained with the aforementioned resolution. The particles orbit will only change due to changes in the direction of the magnetic field and the guiding centre approximation is an accurate description of the particle dynamics. The major advantage of this approach is that the time step taken in the simulations can be several orders larger in comparison with solving the full equation of motion. Initially, particles have a Maxwellian velocity distribution for $v = \sqrt{(v_{\parallel})^2 + (v_{\perp})^2}$. This corresponds to the thermal velocity $v_{th} = \sqrt{(\frac{2k_B T \rho_0}{m_p p_0})}$ of protons in a fluid of temperature about $T = 10^6 K$ with the proton rest mass $m_p = 1.6726 \cdot 10^{-24} g$ and dimensionless pressure p_0 and fluid density ρ_0 as defined in Section 2.1. The particles have a uniform pitch angle distribution with $\alpha \in [-\pi/2, \pi/2]$. Particles are initiated in static MHD snapshots at three different times. Shortly after the start of the linear growth of the tilt instability, at the moment the instability reaches the nonlinear regime and its peak current and far in the saturated, nonlinear regime. The particles are evolved for the typical time $t = t_S = L/c_S \approx 85.26$ seconds, with c_S the sound speed outside the current channels in the MHD snapshots. The MHD quantities are static on the particles timescales and are not evolved. We analyse 200.000 electrons and protons evolved in snapshots $t = 5$, $t = 8$ and $t = 9$ in cases F2dff and F2dffAR, corresponding to $5t_S \approx 417$ seconds, $8t_S \approx 680$ seconds and $9t_S \approx 765$ seconds respectively. After one time, there are particles which are accelerated significantly, such that their gyroradius becomes large, although still small compared to a grid cell of $25000m$. The maximum gyroradius reached in the simulations carried out is $17 \cdot 10^{-2} m$ for electrons and $8.5 \cdot 10^2 m$ for protons, both after $1t_S$. Mainly for protons it is therefore necessary to be cautious about obtained results at late times since gyration effects may become important and cannot be neglected.

We will quantify the particle dynamics by looking at the energy distribution of the whole ensemble of particles, by analysing the relative importance of the separate drifts in particular regions of the domain and by following the evolution of the kinetic energy of individual particles, identified to show interesting behaviour.

Evolving test particles in static MHD snapshots in a 2.5D configuration shows that the dominant processes are particle acceleration in either of the two current channels or acceleration by the resistive electric field in the ambient. Both processes cause a large acceleration in the direction parallel to the magnetic field, which is dominant over all other acceleration and drift processes. This means that either the particles leave the domain through one of the open x, y boundaries, or they are accelerated indefinitely in the current channels, in the translationally invariant z -direction. To counteract this artifact, we also evolve particles in the setups with anomalous resistivity. The particles are then expected not to accelerate due to resistive electric field in the ambient, where resistivity is absent. However, they still will be in the reconnection areas around the current channels and inside the current channels.

The kinetic energy of a particle is $E_k = (\gamma - 1)m_0c^2 \approx m_0c^2(\frac{1}{2}\frac{v^2}{c^2} + \frac{3}{8}\frac{v^4}{c^4})$. In Figures 16-18 the kinetic energy (divided by m_0c) distribution counted by number of particles is shown for both electrons (in the left panels) and protons (in the right panels), normalised by the total number of particles, at $t = 5$ before the linear growth phase of the instability, $t = 8$ at the end of the linear growth phase and $t = 9$ in the strongly nonlinear regime. The total number of bins is set to the square root of total number of particles, on a logarithmic scale. The distribution is plotted in every panel at representative time intervals up to $1t_S$, indicated in the colour bar on the right. The electron dynamics are much faster and a high energy tail already develops withing $0.1t_S$, whereas the proton dynamics are slower, in accord with the mass difference. The spectra are initially purely thermal, but all quickly develop a middle part at medium energy and a high energy tail.

At $t = 5$, the high energy tail developing is mainly due to acceleration parallel to the magnetic field, for $\gamma - 1 > 1$. Because of uniform resistivity there is a parallel, resistive electric field in the whole domain, accelerating particles accordingly. There is a medium tail forming as well between the thermal distribution and the high energy tail, for $10^{-5} < \gamma - 1 < 10^0$. Parallel acceleration due to resistive electric field is the dominant mechanism compared to the drift terms in equation (14). At $t = 8$ and $t = 9$ in Figures 17 and 18 for electrons and for protons, particles are still accelerated up to very high energies ($\gamma \sim 10^4$) due to parallel acceleration, but a more pronounced tail has developed at medium energies as well $\gamma \sim 1 - 10^2$ due to other acceleration mechanisms. This middle part of the spectrum reaches a Lorentz factor of maximum 1.5 to 2 times the thermal Lorentz factor $\gamma = 1$, confirming the findings of Zhou et al. (2015) for acceleration due to magnetic curvature drifts and magnetic gradient drifts perpendicular to the magnetic field.

Particles, mainly trapped inside the current channels but also in the ambient, reach extremely high energies due to indefinite acceleration in the translationally invariant z -direction due to the 2.5D nature of the simulations. This numerical artifact is counteracted by employing the anomalous resistivity model described by equation (9). In this case (F2dffAR) there is no resistivity, and hence no parallel electric field $E_{\parallel} = \eta \mathbf{J} \cdot \hat{\mathbf{b}}$, in regions with a low current (low meaning equilibrium values). Particles are now still accelerated indefinitely in the invariant z -direction, but not anymore due to resistive electric fields in the ambient. In general protons and electrons behave similarly, with the main difference that protons are much slower due to the difference in mass. It takes a longer time for protons to form a smooth high energy tail and the maximum Lorentz factor

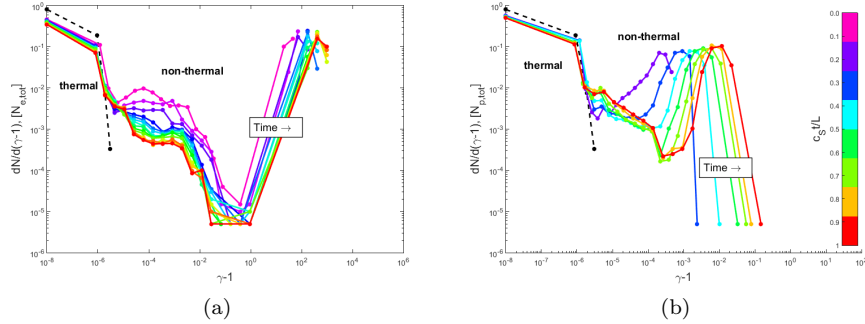


Figure 16: Kinetic energy distribution counted by particle number at $t = 5$ plotted up to $t = 6$ for 200.000 electrons (left panel) and protons (right panel) for equilibrium F2Dff. Time is measured in units of L/c_s , see the colour bar at the right, with $L = 10 \cdot 10^6 m$ and c_s the speed of sound. The initial Maxwellian is depicted with a dashed, black line, showing the thermal part of the distribution.

reached is two orders of magnitude smaller than for electrons in all cases.

The high energy particles dominate not only in number, seeing that almost all particles pick up a parallel acceleration at later times, they also dominate in energy. This can be seen from Fig. 19 where the kinetic energy distribution is plotted at $t = 8$, now not counted by the number of particles but by the kinetic energy of the particle. The high energy tail is now even more pronounced at all times, both for protons (right panel) and electrons (left panel). The plasma energy content is dominated by the particles at high energy, contrasting with the expected energy spectrum in which low energy particles dominate both by number and energy (Rosdahl and Galsgaard 2009).

The expected effect of anomalous resistivity on particle acceleration is that less particles are accelerated by resistive electric field, since it is not present uniformly anymore. This avoids strong particle acceleration in the ambient, meaning that particles can still accelerate up to high energies, but high energy particles should not dominate in number anymore. This effect can be observed from the kinetic energy distributions. In Fig. 20 the number distribution is plotted and both for electrons and protons there is still a second high energy tail due to parallel acceleration, but it is less dominant than in the case with uniform resistivity. However, in Fig. 21, for the same case, the kinetic energy distribution is plotted and the high energy particles are even more dominant in energy. Due to the anomalous resistivity present only in regions with strong current, large gradients in the electromagnetic fields arise. A larger peak current is reached, already concluded from the MHD simulations, and particles are accelerated up to even higher kinetic energy ($\gamma \sim 10^6$ for electrons and $\gamma \sim 0^2$ for protons). We conclude that with uniform resistivity applied, high energy particles are dominant in the energy distribution both in number and counted by energy per particle. Whereas with anomalous resistivity applied, high energy particles are mainly dominant in the energy distribution counted by energy but less in number.

The peak energy reached in these simulations based on 2.5D MHD runs is orders of magnitude larger than expected from observations of particles ac-

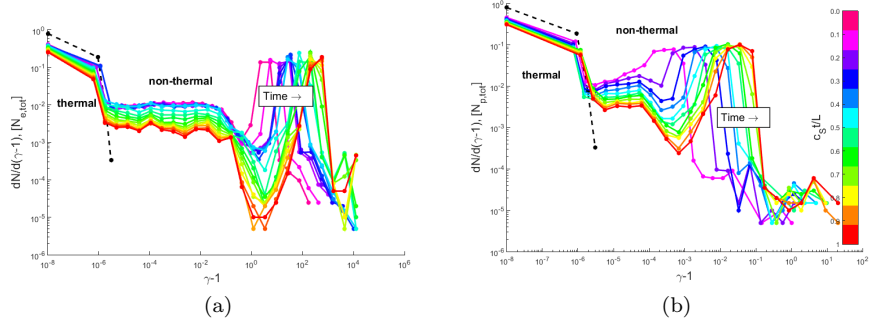


Figure 17: Kinetic energy distribution counted by particle number at $t = 8$ plotted up to $t = 9$ for 200.000 electrons (left panel) and protons (right panel) for equilibrium F2Dff. The initial Maxwellian is depicted with a dashed, black line, showing the thermal part of the distribution.

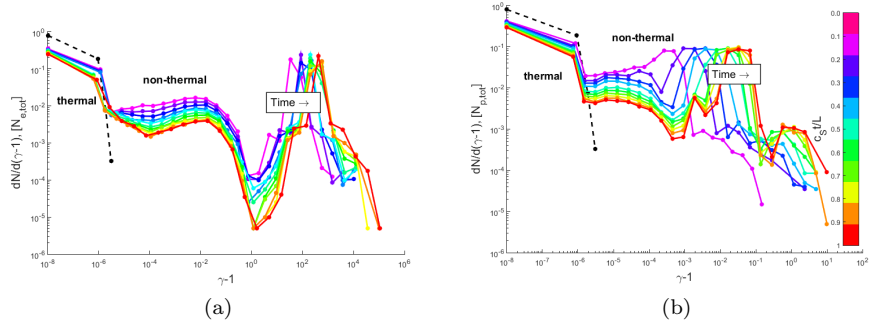


Figure 18: Kinetic energy distribution counted by particle number at $t = 9$ plotted up to $t = 10$ for 200.000 electrons (left panel) and protons (right panel) for equilibrium F2Dff. The initial Maxwellian is depicted with a dashed, black line, showing the thermal part of the distribution.

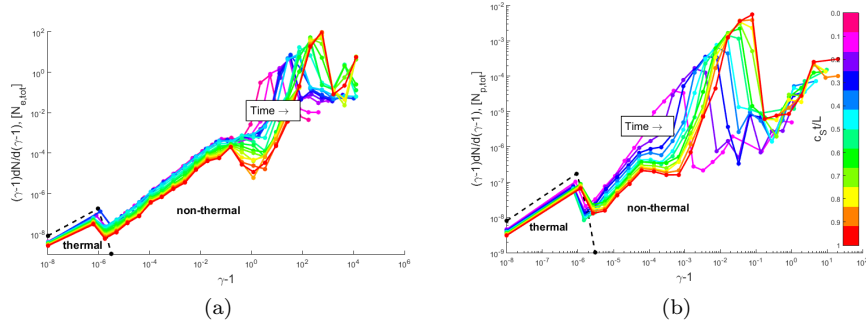


Figure 19: Kinetic energy distribution counted by particle energy at $t = 8$ plotted up to $t = 9$ for 200.000 electrons (left panel) and protons (right panel) for equilibrium F2Dff. Time is measured in units of L/c_s , see the colour bar at the right, with $L = 10 \cdot 10^6 m$ and c_s the speed of sound. The initial Maxwellian is depicted with a dashed, black line, showing the thermal part of the distribution.

celeration in solar flares (Rosdahl and Galsgaard 2009). This effect is mainly due to the high resistivity $\eta = 10^{-4}$ (more realistic, lower values would severely limit the computation time and no longer minimise the numerical dissipation for MHD evolutions), and the subsequent electric field accelerating particles in the direction parallel to the magnetic field. Neglecting the second high energy tail caused by parallel acceleration in the current channels, electrons reach maximum Lorentz factors of $\gamma \sim 2$ and protons of $\gamma \sim 1.01$, in the reconnection zones in both cases, and these values are more realistic for the solar corona.

The dominance of parallel acceleration is also depicted by the spatial pitch angle distribution $\alpha = \arctan(v_{\perp}^*/v_{\parallel})$, in Fig. 22 for electrons in setup F2dff and in Fig. 23 for protons in setup F2dffAR, plotted on top of the absolute value of the resistive electric field as obtained from MHD, as an indicator of reconnection regions (see Figures 6 and 7 for the respective resistive electric field without particles plotted on top). In the regions with strong resistive electric field (marked by yellow background colour in Fig. 23) the pitch angle is small, as expected, however, also in the current channels (with absent resistive electric field, indicated by the grey background colour) the pitch angle is close to zero (indicated by the particles coloured white) already shortly after the particles are initialised. The dominance of the resistive electric field acceleration makes high energy electrons move antiparallel to the magnetic field and high energy protons parallel to the magnetic field. In a setup with anomalous resistivity, this is still the case. The anomalous resistivity solves the issue of parallel acceleration in regions without a high current, but not in the current channels. The particles are even accelerated up to higher energies due to the higher peak current reached in the case with anomalous resistivity. Therefore at $8t_S + 0.05t_S$, the particles have travelled further into the current channels (in the direction perpendicular to the plane shown). Particles are dragged into the current channels from regions where resistivity, and hence parallel electric field is absent. This is visualised by the ‘gaps’ in Figures 23 and 25 for case F2dffAR, with anomalous resistivity, where no particles are present anymore in the areas without resistive electric field around the current channels, but energetic particles (with $\alpha \approx 0$ and large

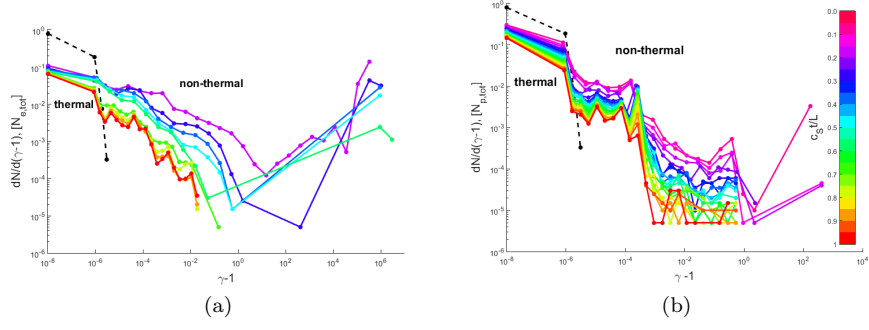


Figure 20: Kinetic energy distribution counted by particle number at $t = 8$ plotted up to $t = 9$ for 200.000 electrons (left panel) and protons (right panel) for equilibrium F2DffAR. The initial Maxwellian is depicted with a dashed, black line, showing the thermal part of the distribution.

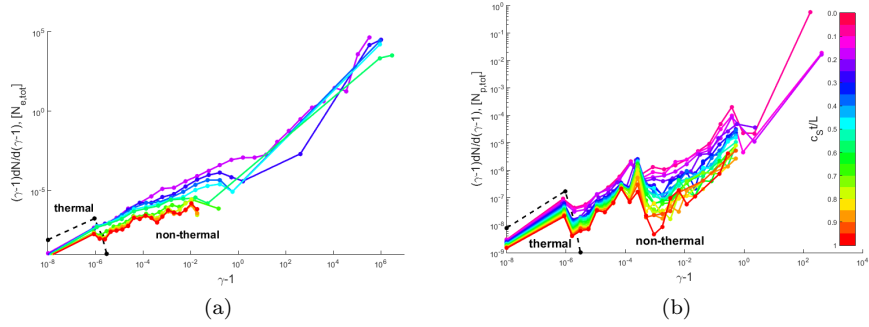


Figure 21: Kinetic energy distribution counted by particle energy at $t = 8$ plotted up to $t = 9$ for 200.000 electrons (left panel) and protons (right panel) for equilibrium F2DffAR. The initial Maxwellian is depicted with a dashed, black line, showing the thermal part of the distribution.

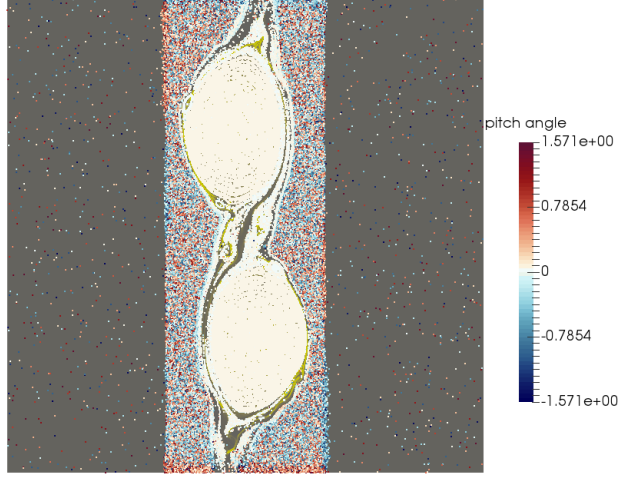


Figure 22: Spatial distribution of pitch angle α at $8t_S + 0.05t_S$ for electrons in case F2dff. Particles are visualised as dots plotted on top of the magnitude of the parallel electric field as obtained from MHD, where the yellow coloured parts indicate a nonzero parallel electric field and hence reconnection occurring, and grey parts indicate absent parallel electric field (see Fig. 6 for the resistive electric field without particles plotted on top). For the parallel electric field a linear colour is saturated to show values between $[0, 0.001]$. Particles in and around the current channels have a pitch angle close to zero (mainly coloured white) and thus a dominant parallel velocity.

parallel velocity) are residing in the current channels.

To analyse the relative importance of the drift terms in the evolution equation of the guiding centre position, we plot the magnitudes of the three dominant vectorial terms in equation (14) in Figures 24 and 25 for 200.000 electrons in a snapshot with uniform resistivity (F2dff) and with anomalous resistivity (F2dffAR) respectively at $t = 8 + 0.05$, again measured in units of the speed of sound t_S . The particles are coloured by magnitude of the, from left to right, $\mathbf{E} \times \mathbf{B}$ drift ($-\hat{\mathbf{b}}/B \times c\mathbf{E}$, the second term on the right-hand-side of equation (14)), the curvature drift ($\frac{\hat{\mathbf{b}}}{B(1-E_\perp^2/B^2)} \times (cm_0\gamma/q)(v_\parallel^2(\hat{\mathbf{b}} \cdot \nabla)\hat{\mathbf{b}})$, the third term on the right-hand-side of (14)) and the parallel velocity ($v_\parallel\hat{\mathbf{b}}$, the first term on the right-hand-side of (14)), normalised by the speed of light c , plotted on top of the absolute value parallel, resistive electric field obtained from the MHD snapshot at $t = 8$, as an indicator of reconnection regions (see Figures 6 and 7 for the respective resistive electric field without particles plotted on top). The spatial distribution of the particles does not change much compared to the initial uniform distribution. Fast particles are trapped inside the current channels, both

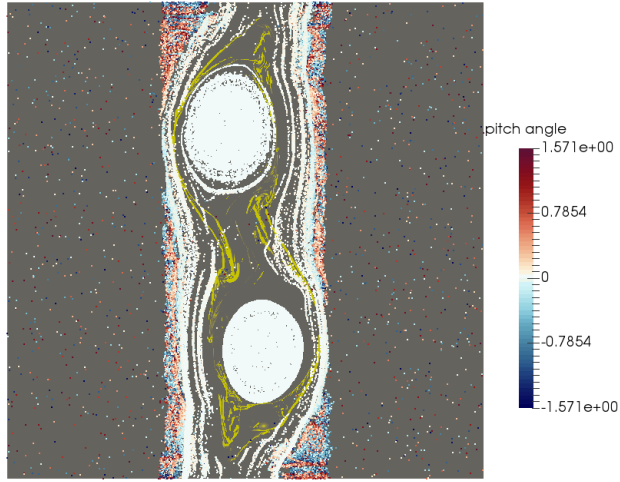


Figure 23: Spatial distribution of pitch angle α for protons at $8t_S + 0.05t_S$ in case F2dffAR. Particles are visualised as dots plotted on top of the magnitude of the parallel electric field as obtained from MHD, where the yellow coloured parts indicate a nonzero parallel electric field and hence reconnection occurring, and grey parts indicate absent parallel electric field (see Fig. 7 for the resistive electric field without particles plotted on top). For the parallel electric field a linear colour is saturated to show values between $[0, 0.001]$. Particles in the current channels have a pitch angle close to zero (mainly coloured white) and thus a dominant parallel velocity.

in the case with uniform and in the case with anomalous resistivity. All particles initially in the rectangular area around the current channels, remain there on the timescales shown. At later times the current channels push the particles a little more outward into the ambient, but the effect is negligible. The particles in the ambient (indicated by the grey background, with absent resistive electric field) remain thermal. In case F2dffAR the particles are pushed away from the regions without resistivity around the current channels due to the higher magnetic field gradients building up. The magnetic islands trap particles even more efficiently in this case, enabling them to reach higher parallel velocities. Particles trapped inside the magnetic islands travel in the z -direction and form jets emerging far into the current channels, reaching high energies. There is a strong correlation between the energy of the particles and the displacement in the z -direction (the direction depends on the current channel and on the charge of the particle). This is another indication that the particle acceleration is dominated by resistive electric field, confirming the results of Zhou et al. (2016) for electron acceleration in 2.5D reconnection in the solar corona.

In regions with strong resistive electric field, particles are accelerated strongly, mainly in the direction parallel to the magnetic field, corresponding to the $v_{\parallel} \hat{\mathbf{b}}$ term in equation (14). However, the relativistic $\mathbf{E} \times \mathbf{B}$ drift (the second term on the right hand side of equation (14)) and the relativistic curvature drift $\mathbf{B} \times \nabla \mathbf{B}$ (the third term on the right hand side of equation (14)) have a non-negligible contribution to particle acceleration. The other drift terms in equation (14) are at least five orders of magnitude smaller. The relative importance of the curvature drift on the total particle velocity is due to the proportionality to v_{\parallel}^2 (see equations (15) and (18)). Zhou et al. (2016) finds similar results, where the curvature drift is less dominant in case the resistive electric field acceleration is neglected and enhanced when parallel electric field is taken into account.

The parallel velocity of the particles trapped inside the current channels grows quickly due to the translational invariance of the in-plane direction. This is a numerical artifact of 2.5D simulations and is also expected to occur in 3D simulations with periodic boundary conditions. The strong resistive electric field, due to the resistivity $\eta = 10^{-4}$, accelerates particles up to Lorentz factors of the order of $10^4 - 10^6$ for electrons and $10^2 - 10^3$ for protons. The particles in the ambient, where no or small resistive electric field has built up, move thermally along magnetic field lines, without significant changes in their kinetic energy.

To gather more insight in the details of individual particle behaviour, few typical examples of particles moving through reconnection regions and the most energetic particles are identified. We show the trajectories (Figures 25 and 24) and the evolution of γ (Figures 28 and 29) for particles trapped inside one of the current channels and for particles moving through the reconnection zones. The most efficient acceleration happens to particles trapped inside the current channels, moving parallel to the magnetic field, reaching Lorentz factors up to $\gamma \sim 10^2$ within $0.01t_S$ to $0.1t_S$ both for protons and electrons. Since the electric field is static in the snapshots taken, the particles Lorentz factor cannot grow faster than $\gamma \sim qEct$ with E the constant amplitude of the electric field. Particles reaching medium energies (Lorentz factor of the order of $\gamma \sim 2$) are observed to undergo repeated acceleration and deceleration passing through reconnecting fields, in accordance with the results of Rosdahl and Galsgaard (2009). This behaviour is observed for particles identified to move through the current sheets. For several particles the temporal evolution of γ is depicted in

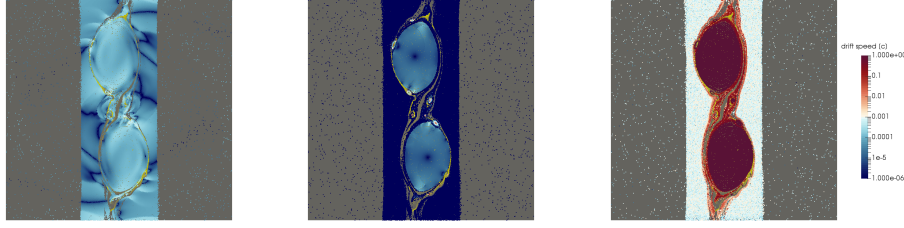


Figure 24: Magnitude of the relativistic $\mathbf{E} \times \mathbf{B}$ drift ($-\hat{\mathbf{b}}/B \times c\mathbf{E}$, the second term on the right-hand-side in equation (14)), the relativistic curvature \mathbf{B} drift ($(\frac{\hat{\mathbf{b}}}{B(1-E_\perp^2/B^2)} \times (cm_0\gamma/q)(v_\parallel^2(\hat{\mathbf{b}} \cdot \nabla)\hat{\mathbf{b}})$, the third term in equation (14)) and the parallel velocity ($v_\parallel\hat{\mathbf{b}}$, the first term in equation (14)) from left to right at $8t_S + 0.05t_S$ in case F2dff. The drifts are normalised to the speed of light and plotted to the same scale. Particles visualised as dots are plotted on top of the magnitude of the parallel electric field as obtained from MHD, where the yellow coloured parts indicate a nonzero parallel electric field and hence reconnection occurring, and grey parts indicate absent parallel electric field (see Fig. 6 for the resistive electric field without particles plotted on top). For the parallel electric field a linear colour is saturated to show values between $[0, 0.001]$. The parallel velocity is clearly dominant compared to the drift velocities.

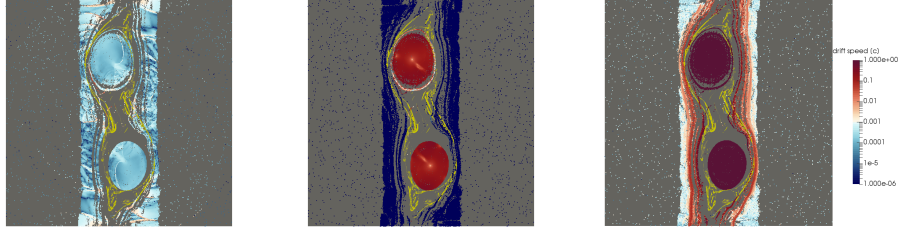


Figure 25: Magnitude of the relativistic $\mathbf{E} \times \mathbf{B}$ drift ($-\hat{\mathbf{b}}/B \times c\mathbf{E}$, the second term on the right-hand-side in equation (14)), the relativistic curvature \mathbf{B} drift ($(\frac{\hat{\mathbf{b}}}{B(1-E_\perp^2/B^2)} \times (cm_0\gamma/q)(v_\parallel^2(\hat{\mathbf{b}} \cdot \nabla)\hat{\mathbf{b}})$, the third term in equation (14)) and the parallel velocity ($v_\parallel\hat{\mathbf{b}}$, the first term in equation (14)) from left to right at $8t_S + 0.05t_S$ in case F2dffAR. The drifts are normalised to the speed of light and plotted to the same scale. Particles visualised as dots are plotted on top of the magnitude of the parallel electric field as obtained from MHD, where the yellow coloured parts indicate a nonzero parallel electric field and hence reconnection occurring, and grey parts indicate absent parallel electric field (see Fig. 7 for the resistive electric field without particles plotted on top). For the parallel electric field a linear colour is saturated to show values between $[0, 0.001]$. Compared to Fig. 24 the curvature drift inside the current channels has gained importance.

Fig. 28 for electrons at $t = 8t_S$ to $t = 8t_S + 0.1t_S$ in case F2dff and in Fig. 29 for protons at $t = 8t_S$ to $t = 8t_S + 0.01t_S$ in case F2dffAR. Dashed lines growing linearly in time are plotted to guide the eye. The repetitive acceleration and deceleration is stronger in cases with anomalous resistivity, due to the evolution of regions with zero resistivity and hence no resistive electric field to accelerate the particles, and regions with resistivity causing strong gradients in the fields and hence a strong resistive electric field to accelerate the particles again. The trajectories of the selected particles are shown in Fig. 24 and Fig. 25 for electrons in the setup with uniform resistivity and for protons in the setup with anomalous resistivity respectively, plotted on top of the magnitude of the parallel electric field as obtained from MHD. Again, the yellow coloured parts indicate a nonzero parallel electric field and hence reconnection occurring, and grey parts indicate absent parallel electric field (see Figures 6 and 7 for the respective resistive electric field without particles plotted on top). The particles reaching medium γ are located in the current sheets and reconnection zones, whereas the particles reaching higher γ are trapped inside the current channels or in the secondary islands, confirming the picture obtained from the energy distributions.

6 Conclusions

The first part of this work treats the numerical analysis of reconnection induced by a tilt instability in 2.5D setups and the interaction of a tilt and a kink instability in 3D setups. The resistive MHD equations have been solved in plasmas with very high to very low plasma- β and for force-free and non-force-free equilibrium configurations. In all cases the instability grows linearly and causes reconnection. The onset of the instability and the peak currents reached depend on the initial setup strongly, but the general behaviour is similar in all cases. For a force-free setup, the instability grows faster and starts earlier for lower plasma- β , confirming the low resolution results of Richard et al. (1990). For a non-force-free setup, with a constant guide field in the z -direction and a nonzero pressure gradient, the trend is opposite. The tilt instability occurs earlier for higher plasma- β , confirming results of Keppens et al. (2014). Our high resolution results allow us to follow secondary island formation in the regions with strong currents. The effect of a kink instability, in 3D configurations, can enhance or delay the tilt instability depending on the strength of the guide field B_z in non-force-free cases. In force-free setups B_z is chosen such that there is no pressure gradient and the equilibrium holds for the whole range of plasma- β . The kink instability occurs in all force-free cases but the magnetic tension in the z -direction delays the tilt instability compared to the 2.5D with similar plasma- β .

In all cases magnetic reconnection is prone to efficiently accelerate particles. We chose a force-free setup with the lowest plasma- β considered to meet the conditions in the solar corona most realistically. We ran this case both with uniform resistivity and anomalous resistivity only present in regions with a strong current (sufficiently high such that there is no resistivity in the equilibrium phase), to show the effect of resistivity on reconnection. In both cases nearly-singular current sheets and secondary islands form in the high resolution 2.5D runs, but the results are different in the non-linear regime. In the case with

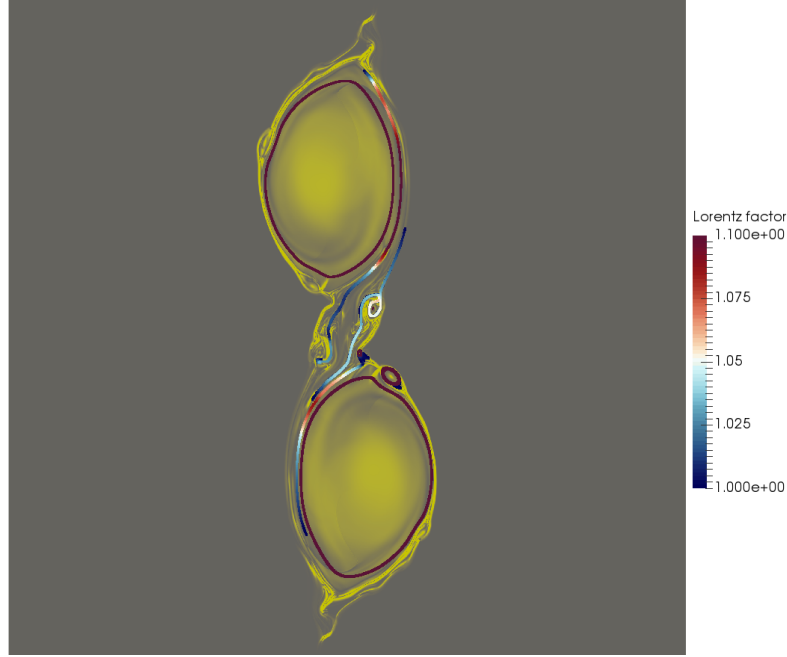


Figure 26: Selected electron trajectories, coloured by their Lorentz factor γ , in a snapshot with uniform resistivity from $8t_S$ to $8t_S + 0.1t_S$. Again plotted on top of the magnitude of the parallel electric field as obtained from MHD, where the yellow coloured parts indicate a nonzero parallel electric field and hence reconnection occurring, and grey parts indicate absent parallel electric field (see Fig. 6 for the resistive electric field without particles plotted on top). For the parallel electric field a linear colour is saturated to show values between $[0, 0.001]$. The same particles are used in Fig. 28 to quantify $\gamma(t)$. These particles belong to the non-thermal kinetic energy population.

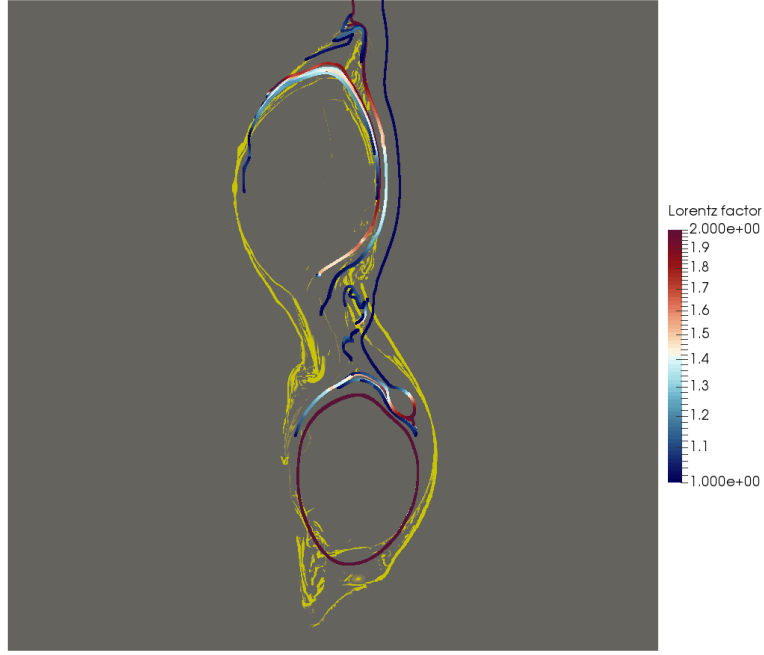


Figure 27: Selected proton trajectories, coloured by their Lorentz factor γ , in a snapshot with anomalous resistivity from $8t_S$ to $8t_S + t_S$. Again plotted on top of the magnitude of the parallel electric field as obtained from MHD, where the yellow coloured parts indicate a nonzero parallel electric field and hence reconnection occurring, and grey parts indicate absent parallel electric field (see Fig. 7 for the resistive electric field without particles plotted on top). For the parallel electric field a linear colour is saturated to show values between $[0, 0.001]$. The same particles are used in Fig. 29 to quantify $\gamma(t)$. These particles belong to the non-thermal kinetic energy population.

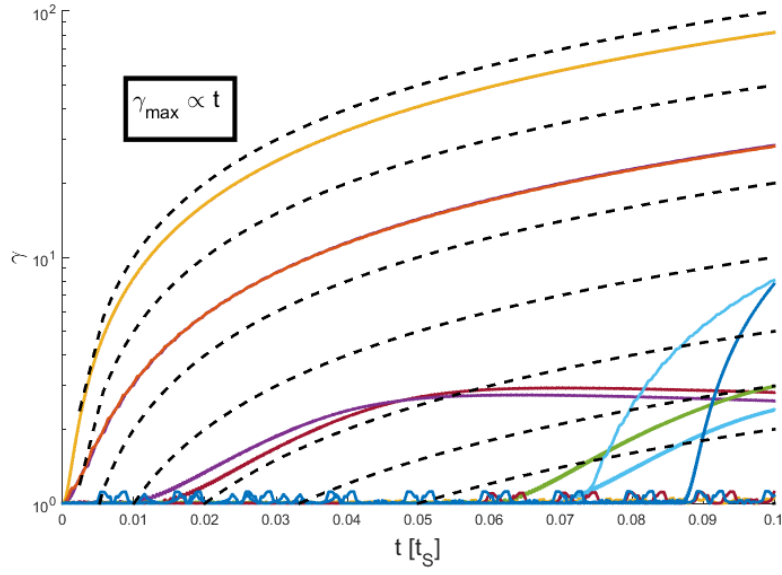


Figure 28: $\gamma \propto t$ for selected electrons in a snapshot with uniform resistivity from $8t_S$ to $8t_S + 0.1t_S$. These particles belong to the non-thermal kinetic energy population. Note the difference for particles mainly affected by parallel acceleration (quickly growing $\gamma(t)$), versus those that repeatedly visit reconnection regions (fluctuating $\gamma(t)$). All particles located in the reconnection zones (secondary islands and thin current sheets) are also shown in Fig. 26 as well as two particles located inside the two current channels.

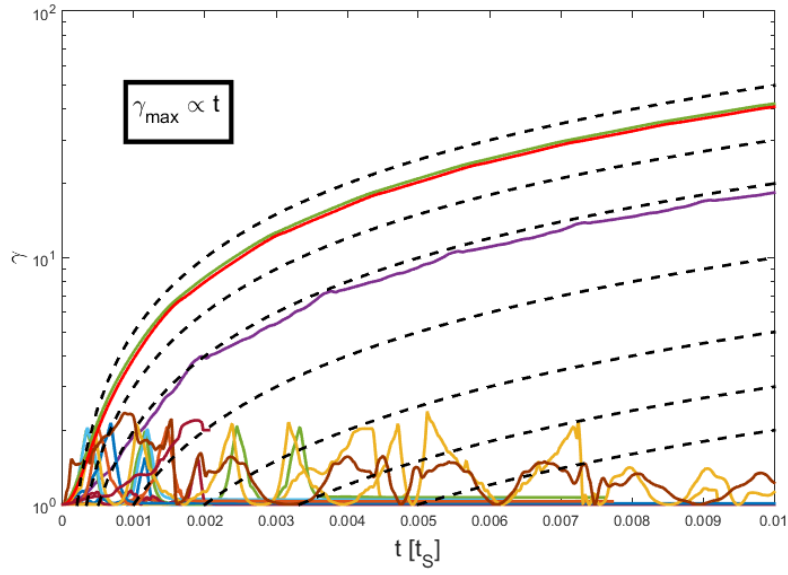


Figure 29: $\gamma \propto t$ for selected protons in a snapshot with anomalous resistivity from $8t_s$ to $8t_s + 0.01t_s$. These particles belong to the non-thermal kinetic energy population. Note the difference for particles mainly affected by parallel acceleration (quickly growing $\gamma(t)$), versus those that repeatedly visit reconnection regions (fluctuating $\gamma(t)$). All particles located in the reconnection zones (secondary islands and thin current sheets) are also shown in Fig. 27 as well as one particle located inside the bottom current channel.

anomalous resistivity a higher peak current is reached due to magnetic gradients that can build at places where there is a transition from nonzero resistivity to zero resistivity. As is well known, from 2.5D MHD simulations (Rosdahl and Galsgaard 2009, Zhou et al. 2016), test particles accelerate in the direction of the magnetic field, due to the presence of a parallel, strong, resistive electric field and on top of that, particles can accelerate indefinitely in the translationally invariant direction. We chose to evolve particles in static MHD snapshots of the 2.5D simulation with lowest plasma- β to analyse how the issue of indefinite acceleration in the z-direction can be tackled for future 3D setups with periodic boundary conditions and 2.5D setups in which the electric and magnetic fields are not constant (i.e. particles evolved simultaneously alongside the MHD evolution and not in static snapshots). A strategy based on anomalous resistivity alone did not yet avoid the artificial build-up of an extreme high energy tail.

We have analysed the behaviour and dynamics of test particles in MHD snapshots from a tilt instability, with uniform resistivity applied, causing magnetic reconnection. We found that both electrons and protons are accelerated efficiently in reconnection zones starting from a Maxwellian distribution function developing a high energy tail. Particles residing inside the current channels are trapped due to the magnetic field structure and due to the 2.5D setup of the simulation, the infinitely long current channels can accelerate electrons efficiently and indefinitely, producing a high energy tail. A second type of acceleration that occurred is due to resistive electric fields, parallel to the magnetic field. Particle acceleration is dominated by resistive electric fields compared to all other means of acceleration, causing particles to reach energies up to $\gamma = 10^6$, confirming the results of Zhou et al. (2016). The energies reached are highly sensitive to the resistivity parameter chosen for the MHD simulations. In Zhou et al. (2016) an anomalous resistivity with magnitude $\eta = 0.003$ is chosen for MHD evolutions and an anomalous resistivity with magnitude $\eta = 1.0 \times 10^{-7}$ is chosen for test particle simulations. Particle acceleration is sensitive to the spatial distribution of the resistive electric fields, meaning that particles accelerate strongly parallel to the magnetic field everywhere with non-zero resistivity. In previous studies with PIC methods (e.g. Lyutikov et al. (2016) for relativistic plasmas and Li et al. (2015)) for low- β plasmas) it was found that magnetic curvature was the dominant acceleration mechanism. In all our simulations the contribution of resistive field acceleration is at least one order of magnitude higher than all other means of acceleration in all our simulations. In our case magnetic curvature acceleration is enhanced by the acceleration caused by resistive electric fields parallel to the magnetic fields due to the proportionality to the parallel velocity of particles and is therefore the second most important acceleration mechanism, again in accordance with the findings of Zhou et al. (2016). However, regardless of this, particles developed a medium energy tail $1 < \gamma < 10^2$ due to all other types of acceleration and drifts. This medium tail develops quickly after the onset of reconnection, whereas the high energy tail due to resistive electric fields develops instantly even in (near) equilibrium snapshots. The distribution formed in all cases varies in the peak energy reached, the time needed to accelerate and the fraction of the particles accelerated. To resolve the dominant resistive electric field acceleration, we applied anomalous resistivity, such that resistive electric fields are only present in regions with a current larger than the equilibrium value. The distribution function now changed in the sense that there are still high energy particles dominating in energy, but not dominating

in number anymore. There are less regions with resistive electric fields and hence less particles accelerated. The peak current reached is higher in the AR evolution however, causing the maximum Lorentz factor for both protons and electrons to be even higher in setups with anomalous resistivity.

The effect of particles reaching too high energies due to resistive electric fields can be moderated in several ways. One way is to adopt a fully kinetic approach, however in the full domain considered in our setup that will be computationally expensive and less flexible. Including 3D effects would solve the issue of an invariant z -direction, however, periodic boundary conditions would have the same effect on the indefinite acceleration (limited by the speed of light) of particles. A solution would be to apply a thermal bath for particles leaving the simulation box in the periodic direction. A particle would then enter at the opposite periodic boundary with a random thermal velocity. This would solve the extreme high energy tail in the distribution function and the issue of particles moving far away from the initial location in the x, y -plane in 2.5D simulations. This solution is considered for follow-up work in which particles are evolved in fully 3D MHD setups and for the full MHD simulation period, rather than in static snapshots to analyse the effect of the kink instability and the effect of dynamic electric and magnetic fields. Another solution would be to decouple acceleration from resistive electric fields from all other types of acceleration (magnetic gradients, magnetic curvature, perpendicular electric fields et cetera). This has been done by Zhou et al. (2015) and Zhou et al. (2016). This nicely shows the separate effects, but it does not solve the high energies obtained due to resistive electric field acceleration. The effect of collisions moderates acceleration as well, this has been done by Gordovskyy et al. (2014) in the context of coronal flux loops and has to be considered for future work in less idealised setups.

The grid resolutions used in the MHD simulations are still a lot larger than the gyroradius of the test particles, such that the guiding centre approach is valid. However, there are particles reaching a gyroradius much larger than expected under the physical conditions applied. This is mainly due to the high Lorentz factors reached and by limiting the fast acceleration due to resistive electric fields, this issue will also be solved. However, in follow-up work the full equation of motion (12) should be solved to compare results and to confirm the validity of the guiding centre approximation. This also gives the opportunity to analyse test particle dynamics in relativistic plasma environments like magnetospheres of compact objects, pulsar wind nebulae and active galactic nuclei, where typical gyroradii are comparable in size to the scale of spatial variations of electromagnetic fields.

In the test particle approach, interaction between particles and feedback of the particles on the fields is neglected. This has a few limitations, mainly that there are no collisions between particles, allowing particles to be accelerated more than in a realistic plasma. Even with collisions included the feedback of highly accelerated particles which are not moderated by collisions would severely influence the electromagnetic fields, which in turn affect the acceleration of particles again. The combination of strong resistive electric fields, lack of collisions and the absence of back reaction on the macroscopic fields causes too many particles to reach too high energy. A way to improve this is to go to fully kinetic simulations or instead to evolve particles in particularly interesting regions, like reconnection zones, with a particle-in-cell approach (e.g. Daldorff et al. 2014, Markidis et al. 2014, Markidis et al. 2015, Tóth et al. 2016, Vaidya et al. 2016).

Acknowledgements

This research was supported by projects GOA/2015-014 (2014-2018 KU Leuven) and the Interuniversity Attraction Poles Programme by the Belgian Science Policy Office (IAP P7/08 CHARM). The computational resources and services used in this work were provided by the VSC (Flemish Supercomputer Center), funded by the Research Foundation Flanders (FWO) and the Flemish Government - department EWI. BR likes to thank Fabio Bacchini, Norbert Magyar, Jannis Teunissen, Kirit Makwana and Dimitris Millas for fruitful discussions and comments.

References

- Bai, X., Caprioli, D., Sironi, L., and Spitkovsky, A. (2015). Magnetohydrodynamic-particle-in-cell method for coupling cosmic rays with a thermal plasma: application to non-relativistic shocks. *ApJ*, 809, 55.
- Biskamp, D. (2000). *Magnetic reconnection in plasmas*. Cambridge, UK: Cambridge Univ. Press.
- Browning, P., Gerrard, C., Hood, A., Kevis, R., and Van der Linden, R. (2008). Heating the corona by nanoflares: simulations of energy release triggered by a kink instability. *A&A*, 485, 3.
- Čada, M. and Torrilhon, M. (2009). Compact third-order limiter functions for finite volume methods. *JCoPh*, 228, 4118.
- Clemmow, P. C. W. and Dougherty, J. P. (1969). *Electrodynamics of Particles and Plasmas*. Reading, US: Addison-Wesley.
- Daldorff, L., Tóth, G., Gombosi, T., Lapenta, G., Amaya, J., Markidis, S., and Brackbill, J. (2014). Two-way coupling of a global hall magnetohydrodynamics model with a local implicit particle-in-cell model. *JCoPh*, 268.
- Finn, J. and Kaw, P. (1977). Coalescence instability of magnetic islands. *PhFl*, 20, 72.
- Goedbloed, J. and Poedts, S. (2004). *Principles of magnetohydrodynamics*. Cambridge, UK: Cambridge Univ. Press.
- Gordovskyy, M., Browning, P., Kontar, E., and Bian, N. (2014). Particle acceleration and transport in reconnecting twisted loops in a stratified atmosphere. *A&A*, 561, 72.
- Guo, F., Liu, Y., Daughton, W., and Li, H. (2015). Particle acceleration and plasma dynamics during magnetic reconnection in the magnetically dominated regime. *ApJ*, 806, 167.
- Keppens, R., Porth, O., and Xia, X. (2014). Interacting tilt and kink instabilities in repelling current channels. *ApJ*, 795, 1.
- Landau, L. and Lifshitz, E. (1960). *Electrodynamics of Continuous Media*. Oxford, UK: Pergamon Press.

- Lapenta, G., Markidis, S., Goldman, M., and Newman, D. (2015). Secondary reconnection sites in reconnection-generated flux ropes and reconnection fronts. *Nature*, 11, 8.
- Li, X., Guo, F., Li, H., and Li, G. (2015). Nonthermally dominated electron acceleration during magnetic reconnection in a low- β plasma. *ApJ*, 811, 24.
- Longcope, D. and Strauss, H. (1993). The coalescence instability and the development of current sheets in two-dimensional magnetohydrodynamics. *PhFlB*, 5, 2858.
- Lyutikov, M., Sironi, L., Komissarov, S., and Porth, O. (2016). Particle acceleration in explosive relativistic reconnection events and crab nebula gamma-ray flares. *J. Plasma Phys.*, submitted.
- Markidis, S., Henri, P., and Lapenta, G. (2014). The fluid-kinetic particle-in-cell method for plasma simulations. *JCoPh*, 271, 415.
- Markidis, S., Henri, P., Lapenta, G., Rönmark, K., Meliani, Z., and Laure, E. (2015). The fluid-kinetic particle-in-cell method for plasma simulations. *JCoPh*, 271.
- Markidis, S. and Lapenta, G. (2011). The energy conserving particle-in-cell method. *JCoPh*, 230.
- Noguchi, K., Tronci, C., Zuccaro, G., and Lapenta, G. (2007). Formulation of the relativistic moment implicit particle-in-cell method. *PhPl*, 14.
- Northrop, T. (1963). *The adiabatic motion of charged particles*. New York: Interscience.
- Northrop, T. (1964). The adiabatic motion of charged particles. *Am. J. Phys.*, 32, 807.
- Otto, A. (2001). Geospace environment modeling (gem) magnetic reconnection challenge: Mhd and hall mhd - constant and current dependent resistivity models. *JGR*, 106, A3.
- Pinto, R., Gordovskyy, M., Browning, P., and Vilmer, M. (2016). Thermal and non-thermal emission from reconnecting twisted coronal loops. *A&A*, 585, 159.
- Pinto, R., Vilmer, N., and Brun, A. (2015). Soft x-ray emission in kink-unstable coronal loops. *A&A*, 576, 37.
- Porth, O., Vorster, M., Lyutikov, M., and Engelbrecht, N. (2016). Diffusion in pulsar wind nebulae: an investigation using magnetohydrodynamic and particle transport models. *MNRAS*, 460.
- Porth, O., Xia, C., Hendrix, T., Moschou, S., and Keppens, R. (2014). Mpi-amrvac for solar and astrophysics. *ApJS*, 214, 4.
- Priest, E. and Forbes, T. (2000). *Magnetic reconnection*. Cambridge, UK: Cambridge Univ. Press.

- Richard, R., Sydora, R., and Ashour-Abdalla, M. (1990). Magnetic reconnection driven by current repulsion. *PhFlB*, 2, 488.
- Rosdahl, K. and Galsgaard, K. (2009). Test particle acceleration in a numerical mhd experiment of an anemone jet. *A&A*, 511, 73.
- Schrijver, C., DeRosa, M., Metcalf, T., and et al. (2008). Nonlinear force-free field modeling of solar active region around the time of a major flare and coronal mass ejection. *ApJ*, 675, 1637.
- Tóth, G., Xianzhe, J., Markidis, S., and et al. (2016). Extended magnetohydrodynamics with embedded particle-in-cell simulations of ganymede’s magnetosphere. *J. Geophys. Res. Space Physics*, 121.
- Uzdensky, D. (2016). Radiative magnetic reconnection in astrophysics. In Gonzalez, W. and Parker, E., editors, *Magnetic reconnection*, chapter 12, pages 473–519. Springer, International publishing Switzerland.
- Vaidya, B., Mignone, A., Bodo, G., and Massaglia, S. (2016). A fluid-particle hybrid framework for the pluto code: applications to non-thermal emission in jets. *JPhys: Conference Series*, 719.
- Vandervoort, P. (1960). The relativistic motion of a charged particle in an inhomogeneous electromagnetic field. *Ann. Phys.*, 10.
- Wiegmann, T. and Sakurai, T. (2012). Solar force-free magnetic fields. *Living Rev. Solar Phys.*, 9, 5.
- Zhou, X., Buechner, J., Barta, M., Gan, W., and Liu, S. (2015). Electron acceleration by cascading reconnection in the solar corona. i. magnetic gradient and curvature drift effects. *ApJ*, 815, 6.
- Zhou, X., Buechner, J., Barta, M., Gan, W., and Liu, S. (2016). Electron acceleration by cascading reconnection in the solar corona. ii. resistive electric field effects. *ApJ*, 827, 94.